PRECISION ENGINEERING CENTER

2003 INTERIM REPORT
October 2003

Sponsors:

3M Corporation
Biomachines
Eastman Kodak Company
IBM Corporation
Los Alamos National Laboratory
National Science Foundation
Oak Ridge National Laboratory
Precitech, Inc.
Vistakon, Inc.

Faculty:

Thomas Dow, Editor
Gregory Buckner
Jeffrey Eischen
Karl Falter
Paul Ro
Ronald Scattergood
David Youden

Graduate Students:

Brett Brocato
Nathan Buescher
Stuart Clayton
Karl Freitag
Karalyn Folkert
David Hood
Patrick Morrissey
Nobuhiko Negishi
Witoon Panusittikorn
Travis Randall
Tao Wu

Undergraduate Students:

Ryan Huth
Ryan Staton
Anthony Wong

Staff:

Lara Bodenhamer
Kenneth Garrard
Alex Sohn
Laura Underhill

TABLE OF CONTENTS

METROLOGY

ACTUATION

FABRICATION

1 FABRICATION, DISTORTION, AND METROLOGY OF SHRINK FIT ELECTRICAL CONNECTIONS

Patrick D. Morrissey
Graduate Student
Jeffrey W. Eischen
Associate Professor
Department of Mechanical and Aerospace Engineering

1.1 INTRODUCTION

After running several pulsed-power experiments using the ATLAS design described in previous reports, problems were encountered and thus design changes were needed. There were minor complications with the axial alignment of components during the shrink fit assembly, but more important were the problems associated with axial stability during the experiments themselves. The ATLAS Generation I shrink fit geometry lacked support for various components (namely the liner and glide planes) in the axial direction. This often resulted in slippage during the high-energy experiments, sometimes completely separating electrical connections. There was a need for a more robust geometry, and thus ATLAS Generation II was developed.

The conceptual fundamentals behind ATLAS Generation II are identical to the design of Generation I. Large current pulses (> 10MA) are passed through the liner, resulting in a radial implosion. The liner implodes at speeds on the order of 10-20km/s, contacting a target contained within the liner. Major differences in this design include the following: the use of a mechanical press fit rather than a thermal shrink fit for liner/glide plane assembly, modified liner dimensions and overall geometry, and a new mechanism through which current flows from the liner. A cross section of the original design (Phase I) of ATLAS Generation II is shown in Figures 1 and 2.

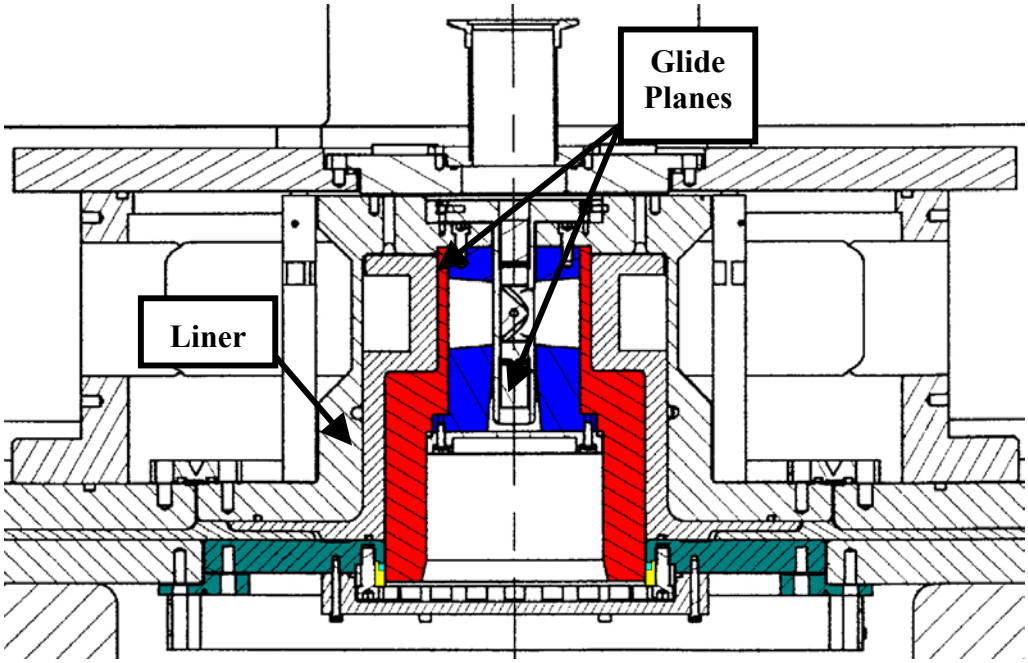

Figure 1. Cross sectional drawing of ATLAS Generation II (Phase I)

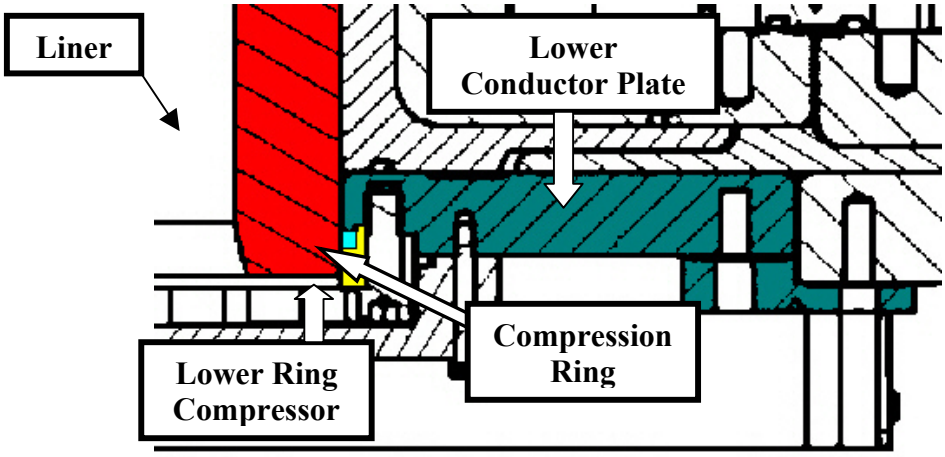

Figure 2. Zoomed view of ATLAS Generation II (Phase I)

One of the major differences of this design is the liner shape. The geometry is no longer cylindrical and lacks the "bump" features on each liner end. The liner dimensions, namely thickness, are easily adjustable during fabrication to meet performance demands determined by experimental parameters (current magnitude, sinusoidal rise-times, etc). Secondly, the upper glide plane is brought into contact with the liner via a mechanical press fit rather than a thermal shrink fit, as in ATLAS Generation I. Finally, the compression ring acts as the new mechanism to transfer current from the liner to the return conductor plates, where the current circuit is completed. The ATLAS Generation I design used the lower glide plane as the current exit route from the liner. Here, the compression ring is slipped over the end of the liner with 0.254mm

(0.010in) of radial clearance. This clearance is compensated for by a sharp tooth on the conductor plate, which distorts the compression ring from the top, thus forcing contact with the liner. The integrity of this interface is vital to the success of the experiments, and therefore the design of the compression ring and its surrounding components (i.e., the liner, ring compressor, and lower conduction plate) are critical. For directional control of current flow, LANL places a high strength insulation tape around the liner OD in areas of close proximity to the lower conduction plate to ensure that the current flows *only* to the compression ring immediately after exiting the liner.

1.2 FINITE ELEMENT ANALYSIS AND RESULTS

Once again the system was modeled with LS-DYNA using axisymmetric elements. The parts surrounding the compression ring were slightly altered by LANL to overcome problems with the experiments, mainly unwanted distortion of other components. One such modification was placement of the tooth on the lower ring compressor that distorts the compression ring from the bottom rather than from the top as described earlier. The geometry of the upper glide plane and liner remained the same through this design transition. The LS-DYNA model of the most recent component geometry is seen in Figure 3.

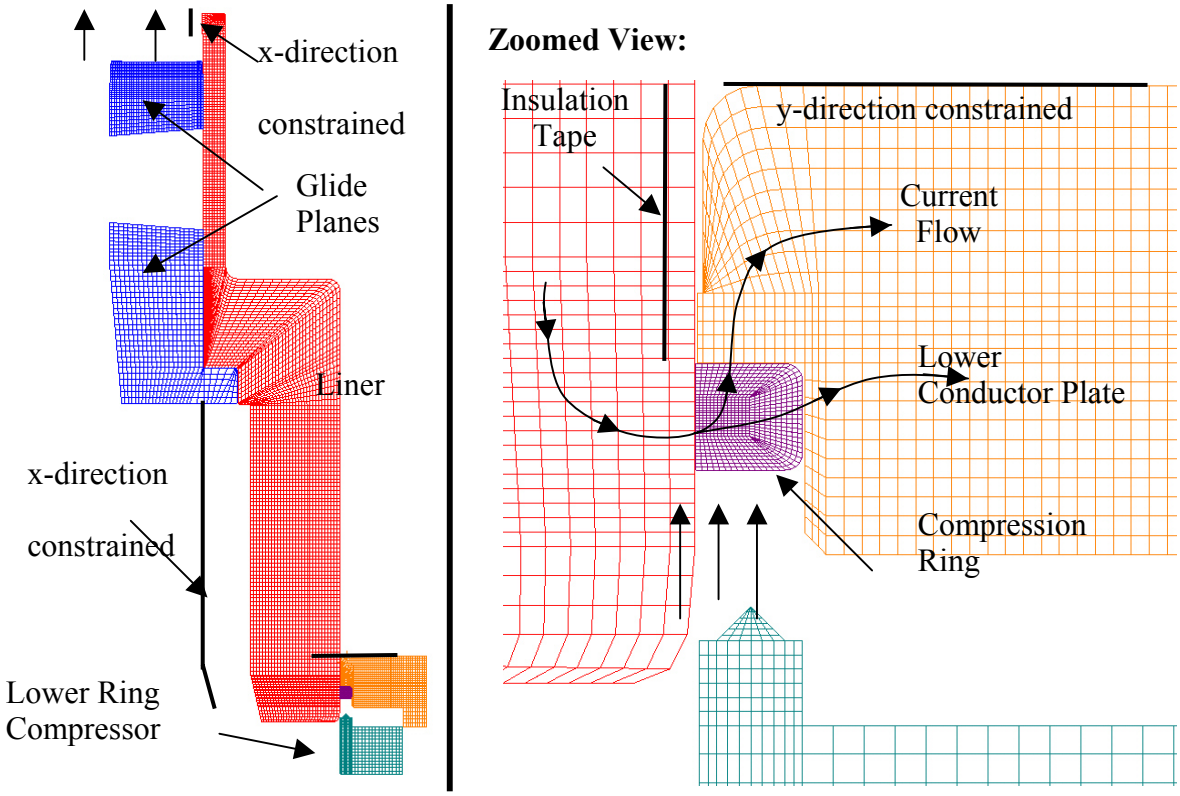

Figure 3. ATLAS Generation II finite element mesh (final design iteration)

The glide planes are composed of copper, the liner and compression ring are 1100 aluminum, the lower conductor plate is 6061 aluminum, and the lower ring compressor is composed of 304 stainless steel.

The six components shown in Figures 1 and 2 are the ones of greatest interest for analysis, and the number of elements used for each of these components is listed in Table 1

Table 1. Number of elements used in the ATLAS Generation II model

Component	# of Elements
Liner	5,002
Small Glide Plane	1,179
Lower Conductor Plate	1,155
Compression Ring	775
Large Glide Plane	774
Lower Ring Compressor	471
Total Elements	*9,356*

1.2.1 RESULTS-UPPER GLIDE PLANE/LINER INTERACTION

During the assembly process, a ring of bolts executes the small glide plane's upward motion and torque specifications are used to indicate the final axial position of the glide plane. A geometric interference created by a radially tapered liner ensures contact with this upper glide plane, which is essential for proper current flow from the glide plane into the liner. To simulate the glide plane's upward motion, a displacement was imposed on a node corresponding to the location of the bolt centerline. An additional, equivalent displacement was imposed on the top node located at the inner radius of this glide plane to prevent detrimental rotation in the FEA model. The locations of these displacement vectors are shown in Figure 3, and the magnitude of these displacements was such that the final axial position of the glide plane mimicked that of the actual assembly. A plot of the radial stress contour for this region can be seen in Figure 4. Note the highly localized stress concentration, which coincides with the relatively small region of radial interference between the two components. Also note the equilibrium of the stress distribution between the two components near this interface.

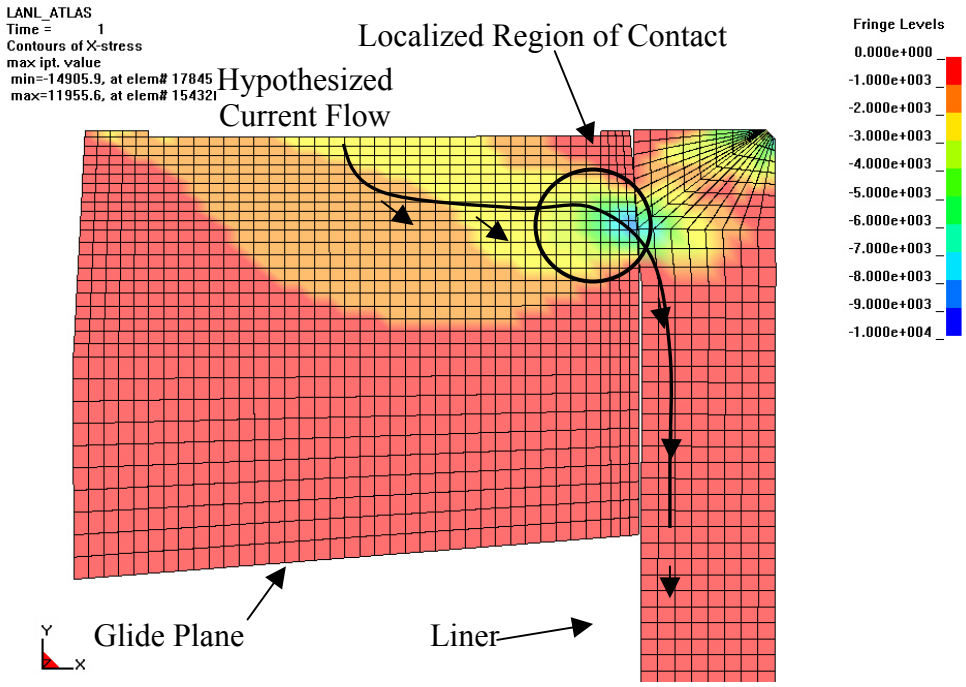

Figure 4. Radial stress (x-stress) of liner/glide plane interface for ATLAS Generation II

The maximum radial stress is approximately 9,500psi. The hoop stress contour plot has a very similar distribution (though not shown) and suggests a maximum hoop stress of approximately 7,700psi. Therefore, some localized yielding occurs in the 1100 aluminum liner, but not in the mating glide plane.

1.2.2 RESULTS-COMPRESSION RING/LINER INTERACTION

During these pulsed-power experiments, the current flows from the top glide plane to the liner, and exits the liner via the compression ring. The integrity of the contact between the compression ring and the liner is contingent on the action of the lower ring compressor. A sharp tooth located on the ring compressor acts as a mechanism to distort the compression ring, thus forcing contact with the adjacent liner. A contour plot of the radial stress is shown in Figure 5. The stress distribution and magnitude in the radial direction were used to gauge the contact integrity of the compression ring's y-faces (interfaces ① and ②), whereas the axial stress distribution and magnitude were used to gauge contact of the ring's x-face (interface ③).

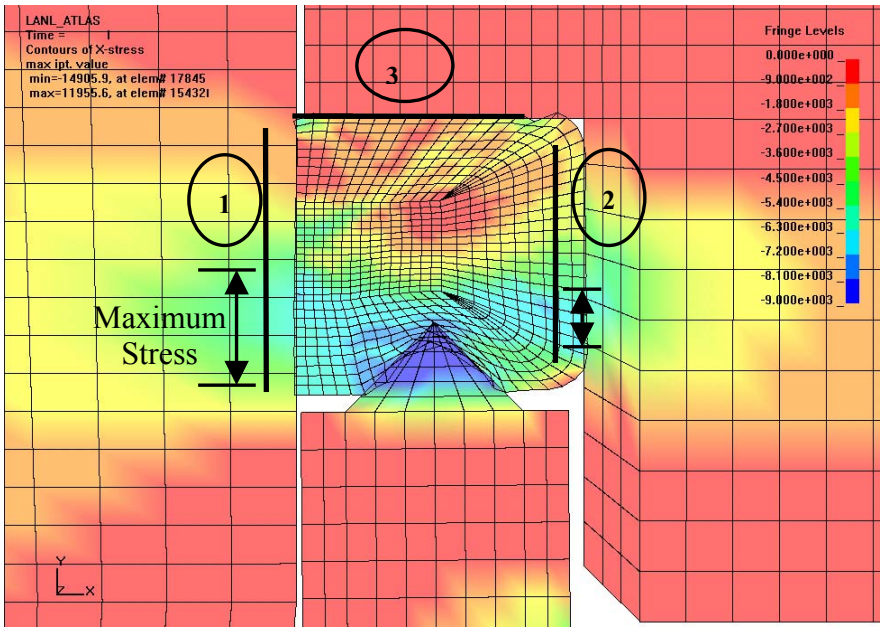

Figure 5. Radial stress (x-stress) in the compression ring for ATLAS Generation II

The stress level in the y-faces of the compression ring is a maximum at the regions near the tooth of the ring compressor. Moving in the positive y-direction along these same faces yields smaller radial stresses. Such a trend suggests a tapered compression ring, which indeed coincides with the shape of the ring compressor's tooth. It is clear that the tooth directly affects the stress levels along each interface, and therefore alternative shapes for this feature were investigated. Since current flows through each of these three interfaces as illustrated in Figure 4, it is important to maximize the level of contact in these regions. By altering the shape of this tooth and investigating the average stress x-stress along interface ① and ②, and the average y-stress along interface ③, it can be determined which geometry changes should be made. This investigation could be used to possibly enhance the effectiveness of these pulsed-power experiments.

1.3 CONCLUSIONS

Finite element analysis of the Atlas Generation II liner/glide plane system has been carried out successfully. The focus of the analysis was on the stress distribution in the vicinity of the upper glide plane/liner joint and on the stress and deformation distribution in the vicinity of the compression ring/liner joint.

2 CHARACTERIZING RESIDUAL STRESS IN SCRIBES ON SILICON USING DEFLECTION MEASUREMENTS

Supplemented With Raman Characterization

Travis Randall
Graduate Student
Dr. Ronald Scattergood
Professor
Materials Science and Engineering

2.1 INTRODUCTION

A scribing apparatus was used to translate a diamond tip across a surface at a constant rate for different loads. With the appropriate conditions, the diamond tip is used to produce scribes on single crystal silicon samples generating brittle-to-ductile transformation of the material beneath the scribe. This anomalous plastic flow has been attributed to a high pressure phase transformation to a metallic β-tin phase.[1] The residual stresses within the scribe traces that result from the elastic-plastic constraint of the displaced material create a bending distortion in a flat-plate geometry wafer sample. The deflection is measured and extracted using optical interferometery techniques. The angle of deflection in the flat plate geometry correlates to the residual stresses created using a bend effect model developed for previous scribing research. Stress approximations will be coupled with Raman, SEM, and AFM characterization to aid in understanding the nature of the material deformation within the scribe zone.

2.2 PROJECT DETAILS

This investigation entails collecting bend data as well as Raman measurements for (100) and (111) crystallographic orientations of silicon, scribing with a Dynatex tip. Scribing along the <100> and <110> will be studied for the (100) orientation. <110> and <112> directions will be studied for the (111) orientation. The deflection angle data will then be correlated to the residual stresses created by scribing using a bend effect model. Indenting was also performed using Vickers and Dynatex tips to study the indentation regions for phase transformation with Raman spectroscopy.

2.2.1 EXPERIMENTAL SETUP

A Zwick micro hardness tester is fitted with a Dynatex diamond tip (Figure 1a) in a custom holder. A motorized stage is used to create translation at a constant rate of 0.250 mm per second.

A holder was designed to hold the cutting edge of the diamond tip at an angle of 3.3 degrees from the sample surface as shown in Figure 1b. The desired load is placed on the loading sleeve and the tip is positioned and contacted to the surface of the sample. The stage is translated with relation to the diamond tip producing the scribe. This setup can achieve repeatable loading below 50 mN and with relatively easy tip alignment in the translation direction.

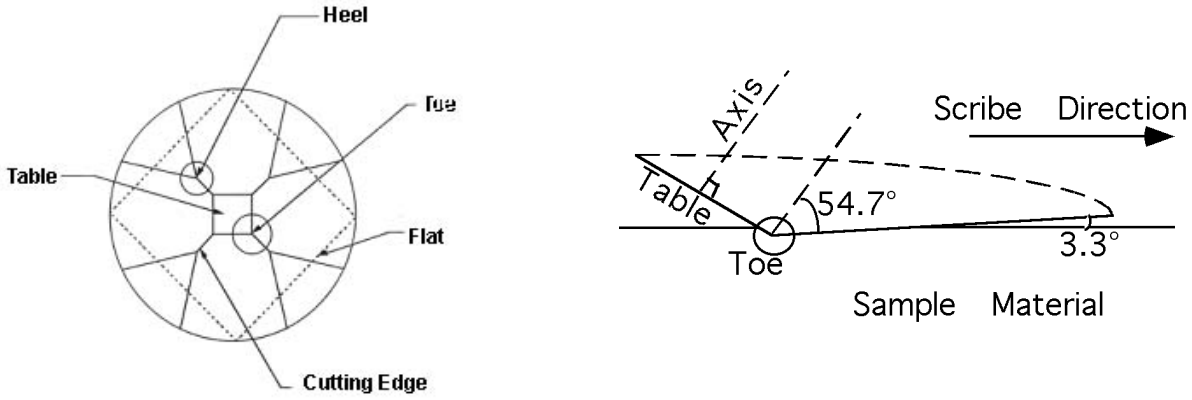

Figure 1. (a) Schematic of Dynatex Tip (b.) Geometry of Tip Relative to Surface [2]

Topographic data is collected for a 1 cm x 2 cm x 525 μm sample using a ZygoGPI Laser interferometer before and after scribing. Multiple, evenly spaced (50-100 μm) scribes are placed on the surface to generate measurable deflection (the effects of multiple scribes are additive to the bend) and to produce a more statistically significant measurement than that of a single scribe. Metropro, the software suite used to analyze the interferometer data, allows the user to subtract the data collected before scribing from that collected after scribing. The resulting profile created is the net bending effect. The profile is then used to approximate the angle of deflection from the initial state.

Characterization of the scribe/indent region was accomplished with Micro-Raman spectroscopy done at room temperature using an ISA U-1000 scanning monochromator. Raman excitation was done with the 514.5 nm line of an Argon-ion laser, with a spot size of approximately 3 to 4 μm in diameter. Raman spectra were taken in the 200-600 cm^{-1} range, which contains the characteristic peaks normally associated with crystalline, amorphous, and various metastable crystalline phases seen in other research. [1]

2.2.2 EXPERIMENTAL RESULTS

Scribing with the Dynatex tip across a 2 cm x 1 cm x 525 mm plate of single crystal silicon yields a measurable deflection on the order of tenths of microns. This behavior is seen in of each of the crystallographic directions studied for both orientations if the load applied is enough to produce cutting action in the material.

Figure 2 shows SEM images distinguishing between the two general responses. The image on the left is scribed on (100) silicon in the [011] direction at 5g load and appears to have no fracture around the scribe and cutting action appears plastic. The plastically displaced material, whether driven by the β-tin metallic phase or not, is pushed by the tip into the surrounding elastic material creating residual stress and deflection in the sample geometry. The image on the right was done at 30g load and shows a large amount of fracture. The action of the diamond indenter may create localized stresses at the tip which exceed the fracture limit, but it is unclear how the transformation region affects this. One of the limitations inherent is that with elastic fracture, removal of the plastically deformed regions may be possible and the bend effect model will not accurately give measure of residual stress for scribes. The bend angle will be decreased relative to a fracture-free scribe.

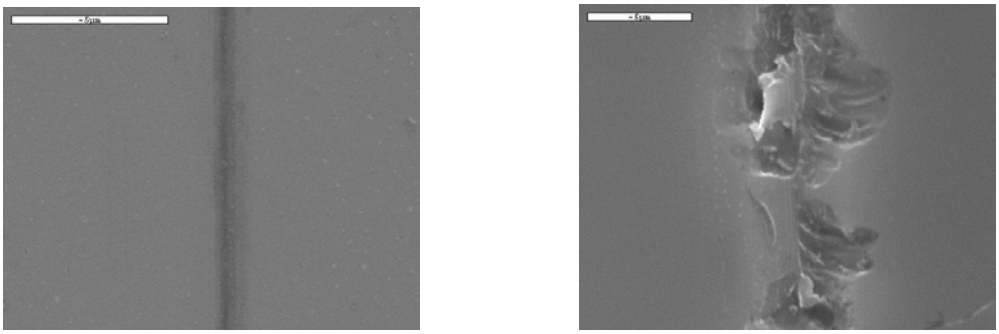

Figure 2. SEM images of scribes (100)[011] at 5g and 30g respectively.

Scribing between 1-20g in the various crystallographic directions with a sharpened tip shows an approximately linear relationship between the normal load applied to the tip and the deflection generated by the residual stresses. Figure 3 shows this trend for (100)[011] and (111)[-1-12], respectively.

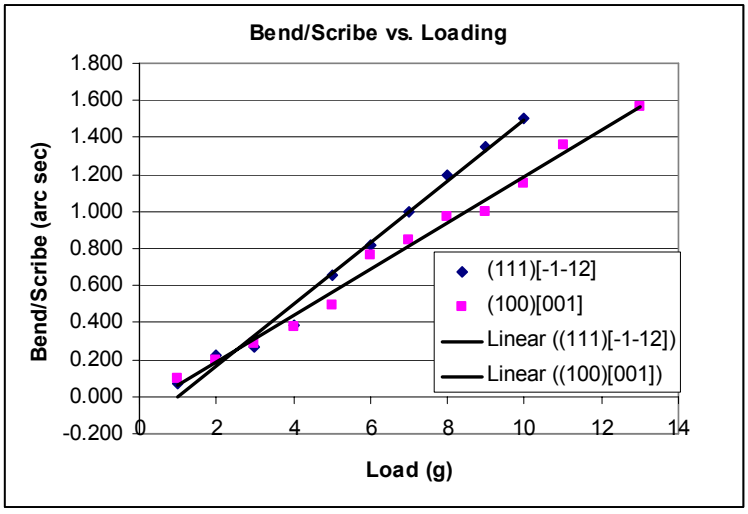

Figure 3. Bend angle generated per scribe versus load applied at tip.

The scribes for the data presented in Figure 3 appear to be fracture free along the scribe traces. This trend could indicate a correlation between the load applied and the amount of plastic deformation occurring beneath the scribe. Experiments for repeatability of these results are currently underway. Other combinations of crystallographic direction and orientation are to be tested.

Experiments using lower loads and a worn tip, 1-10 g, show the appearance of a low-end "threshold" applied load. Below this load, a very apparent drop in visibility of the scribes under optical microscopy occurred. In addition, scribes created at or below this threshold didn't generate measurable deflection, as no residual stress is present. This indicates that no material deformation occurred under the tool tip. Subsequent testing using the same conditions and the same tip for scribing on (100)[011] yielded a shift in threshold to higher loads. Figure 4 is a graph of the load at which the threshold is observed versus the approximate scribe (1cm length) number for that tip face. The figure indicates that the tip needs a higher applied load to achieve the same cutting effect as the tip becomes more worn with subsequent use.

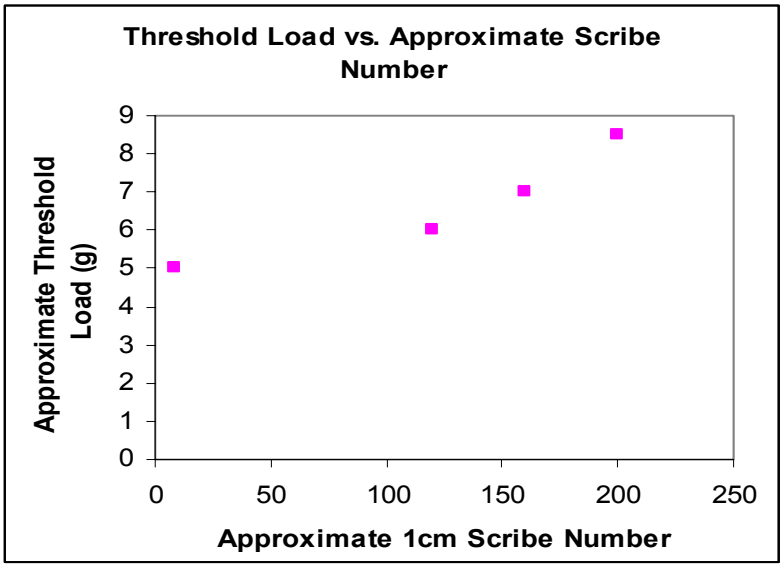

Figure 4. Threshold Load vs Approximate Scribe Number.

Raman was performed on both Vickers scribes (1-15g) and Dynatex scribes (2-40g) with no apparent sign of peaks corresponding to the phases commonly seen after scratching tests. It is not known to the authors at this point why this has occurred. It could be possible that the phase transformation may not be occurring with the Dynatex tip due to the nature of the tip geometry and that the plastic displacement is by some other mechanism, for example, dislocations. It is also possible that the tip may be removing transformed material as it passes. The detection proficiency of the Raman unit may be responsible as well. If the penetration depth of the laser is much greater than that of the transformation zone, or if the laser spot size is large compared to the scribe width, the Raman spectra for the transformation product may not be detected. Sufficient data is not yet available to draw a conclusion for scribing experiments. Indenting

experiments are currently underway to test the Raman unit in indenting conditions already known to generate phase transformation. [1]

2.3 CONCLUSIONS

The bend angle generated due to scribing is on order of arc sec per scribe depending on load applied to the tip. The deflection appears to increase linearly for scribes with minimal fracture, but hasn't shown to be repeatable for specific values of bend angle with similar applied loads. For worn tips bend angle drops dramatically (an order of magnitude) at certain point "threshold." Raman measurements yielded no sign of phase transformation within the scribe regions for both Dynatex and Vickers geometries, contrary to what was anticipated by the authors. This is still being investigated.

2.4 FUTURE WORK

Work continues with using dead-weight loading to create scribe traces with better experimental procedure that aim to improve current data and repeatability. The bend effect model used to correlate sample deflection to an estimate of residual stress within the scribe trace is being tailored to this investigation.

Indenting experiments are currently underway to reproduce the experimental findings of others [1] and gain better insight into the lack of Raman data indicating the expected phase transformations within the scribe region.

Under development is a piezo-actuator driven indenting apparatus. This will aid in performing controlled indents and load control during scribing to test the effects of loading/unloading rate of the tip into the surface.

REFERENCES

1. V. Domnich and Y. Gogotsi. "Phase Transformations In Silicon Under Contact Loading", Rev.Adv.Mater.Sci. 3 (2002) 1-36
2. B. Austin. M.S. Thesis, North Carolina State University, 2000.

3 METROLOGY ARTIFACT DEVELOPMENT

Anthony Wong
Undergraduate Student
Karalyn Folkert
Graduate Student
Thomas Dow
Professor
Mechanical and Aerospace Engineering

3.1 INTRODUCTION

There is an important need to qualify the capability of measuring machines to characterize the dimensional features of 3-D work pieces. Different machines and measurement procedures will produce different results depending on the shape, weight and surface features of the part. Over the years, significant effort has been expended to find methods to calibrate a measuring machine. The methods developed include fixed length ball bars, laser ball bars, ball plates, step gauges, etc. The work volume is typically divided into regions, and the position errors in each region are defined in the x, y and z directions. This error information can be put into look-up tables on the machine controller, and the actual part dimensions can be determined based on the machine measurements plus the errors in position from the error map. The uncertainty in the value of the measurement will involve the error map and the repeatability of that error data for a specific machine position.

Unfortunately, even with the machine calibrated as discussed above, there are a number of errors that can add to the uncertainty of the measurement such as:

- Distortion of the machine due to the weight of the part
- Errors in the probe as a function of the contact angle with the part
- Small perturbations on the part leading to an error in the radius measured
- Probe head errors or lobing

To better quantify the uncertainty of a part measurement, there is a need to create an artifact standard that can be used to "qualify" a measuring machine and probe. The standard would be of a size (radius and wall thickness) that is consistent with the parts of interest, have a similar weight and contain both high and low spatial frequency components that will test the capability of the machine to inspect a class of workpiece shapes.

The goal of this project is to design and fabricate one or more artifacts that can accurately predict the measurement uncertainty associated with the coordinate measuring machines being used at

Y-12. One approach to this problem is to create a standard shape (or several standard shapes) that can be measured on each machine to determine a "transfer function" between the artifact and the measurement. Finding an artifact - or a series of artifacts – to highlight the performance of a specific machine in the Y-12 environment will be an important outcome of this project. Artifacts will be created and measured, and a procedure will be developed to calculate the uncertainty.

In its simplest form, calibration of length dimensions works by using an object, or artifact, of known length and uncertainty and comparing that with measurements from whatever measuring system is being analyzed. For instance, a certified gauge block can be compared to a ruler. As the measuring system becomes more and more complex, the calibration may have to compensate for those complexities. For the CMM shown in Figure 1, the axes of movement are stacked on each other. Both the Z and X axes are mounted on the Y axis bridge. Hence, errors in the Y axis affect the error in the Z and X axes. Such a set up can create Abbe errors. An Abbe error occurs when the measurement axis is not coaxial with the probing axis leading to an amplification of angular errors. For instance, roll of the X axis will produce an error in the y-direction, which will increase as the ram is moved down toward the table. Abbe offsets create non-uniform error within the working volume of the CMM.

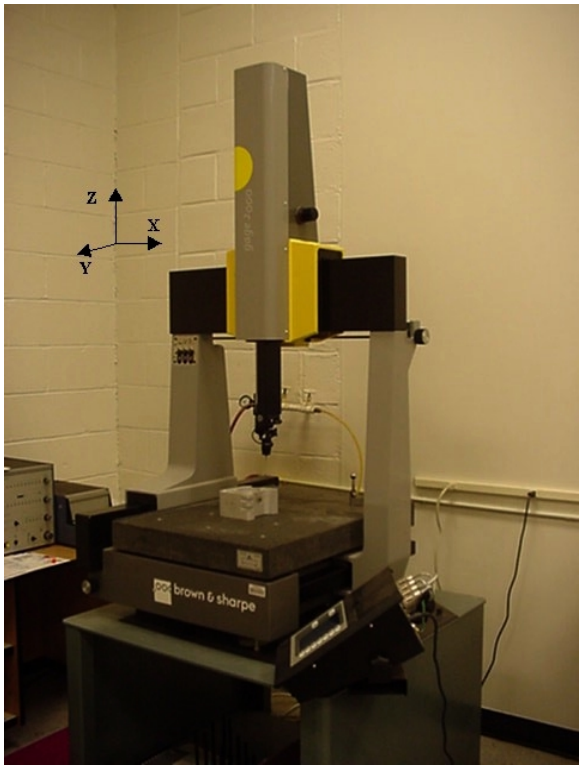

Figure 1. Brown & Sharpe CMM at NCSU

Error mapping the entire working volume of the CMM provides one solution for calibration by correcting the slide position based on the position of the probe. Another approach would be to calibrate the machine for the shape to be measured. If boxes are to be measured, then a box of roughly the same size, shape and weight of the box to be measured is sufficient for calibration. Some other major considerations for an artifact are cost, ease of use, transportability, stability, time needed for calibration and diagnosis of error.

3.2 DETAILS OF THE PROJECT

Based on early discussions of the artifacts needed, a ring gauge was selected as a first approximation. The ring design has a 25 mm square cross-section with an outer diameter of 200 mm. The ring is mounted on three spacers, each 25 mm in diameter and 50 mm long. These spacers mount the ring gauge to a flat 12 mm thick disc that is vacuumed to the chuck of the Diamond Turning Machine (DTM). A sketch of the ring and mounting components is shown in Figure 2. The holes in the ring are counterbored on both sides to allow the ring to be flipped and bolted on the other side. These counterbores are designed for spherical washers that will compensate for any misalignment when the ring is bolted to the spacers. The spherical washers act like a ball and socket joint so that the bolt will not warp the ring if the hole surface is not parallel to the spacer. A frequency analysis was completed using FEM code, and the first five natural frequencies for the disk, spacers and ring are: 1.403 kHz, 1.405 kHz, 2.194 kHz, 2.492 kHz and 2.496 kHz. This should be high enough that the machining frequencies should not create problems.

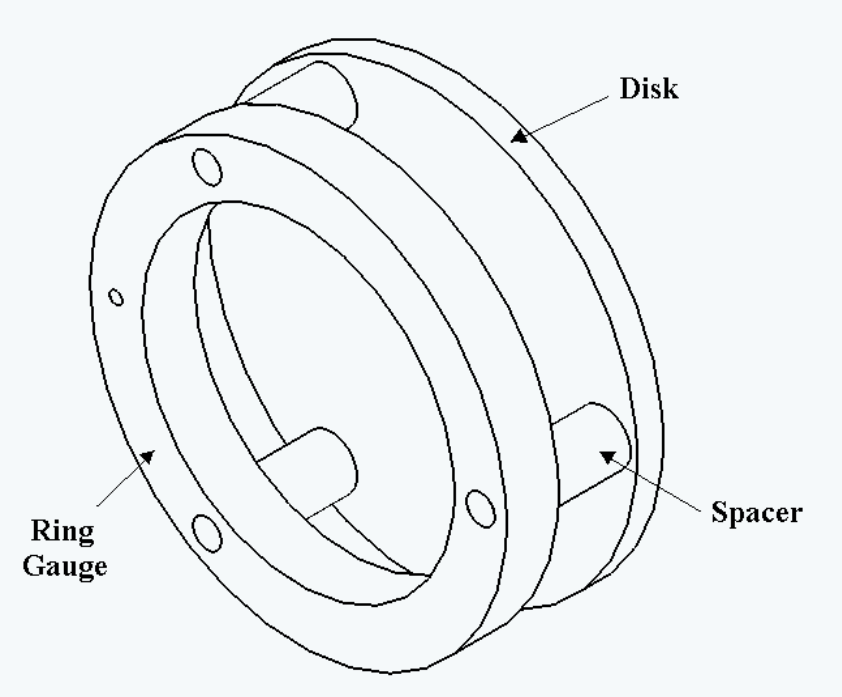

Figure 2. Setup for Mounting to Vacuum Chuck

The resulting ring gauge can be measured on the CMM, and the features of it can be recorded, which include the inside diameter, outside diameter, thickness and surface finish. A comparison among the different machines will provide feedback on the variability of the data generated and some measure of the uncertainty. It can be mounted in several orientations (horizontal, vertical or some intermediate angle), and the effect of the probe angle can be determined.

However, an important component for the artifacts of interest is small features on the surface. These features should contain different magnitudes and spatial frequencies to test the capability of the measuring machine to detect small high-frequency surface features. Such features can be generated with a Fast Tool Servo (FTS). One reason for spacing the ring away from the disk is to allow room to mount the FTS. Figure 3 shows the FTS in place on the machine. This mount will allow the Fast Tool Servo to create features on the inner circumference of the ring.

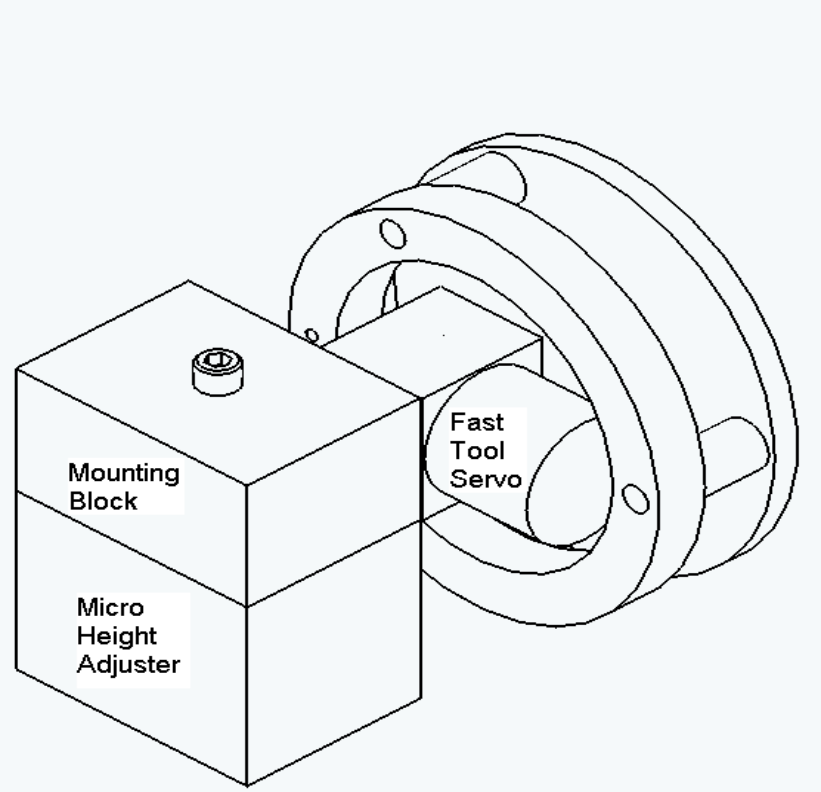

Figure 3. Setup for Diamond Turning a Swept Sine Wave on the ring ID

To fabricate the ring gauge, the disk and spacers are mounted to the chuck and the face of the spacers are machined flat. The ring is attached and the top side is diamond turned; the ring is flipped and the other side is turned. After turning the front and back of the ring, the outer circumference will be turned as a measurement and fiducial surface. Finally, small features will be machined on the ID using the FTS. The first design of these features is a swept sine wave. It is a sine wave where the wavelength is a function of an angle, varying from large to small around the circumference. Figure 4 shows an exaggerated example of what will be machined onto the ring surface – the actual amplitude of the features will be 2.5 μm and the swept sine wave will be "wrapped" around a radius of about 80 mm.

3.3 CONCLUSION

The ring gauge artifact has been designed and is being machined. The details of data format that will be used to generate the swept sine wave are being developed.

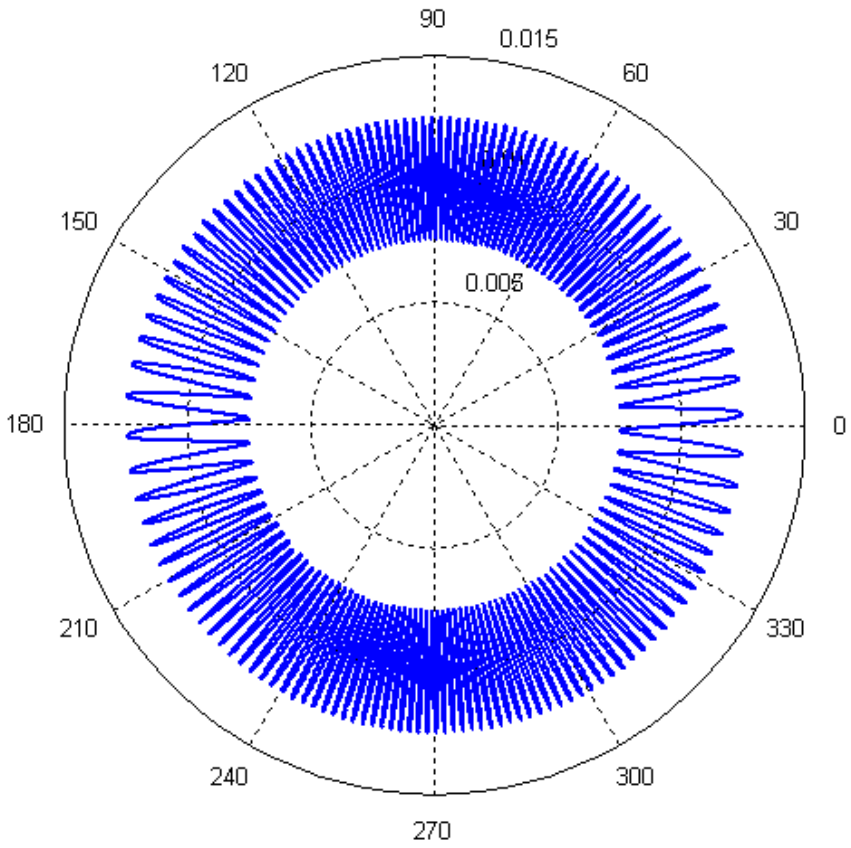

Figure 4. Swept sine wave with the longest wavelength at 0 and 180˚

BIBLIOGRAPHY

1. Cauchick-Miguel, P., King, T., Davis, J. “CMM Verification: A Survey.” Measurement: Journal of the International Measurement Confederation 17.1 (1996):1-16
2. De Aquino Silva, J., Burdekin, M. "A Modular Space Frame for Assessing the Performance of Co-ordinate Measuring Machines (CMMs)." Precision Engineering 26.1 (2002): 37-48
3. Lim, C., Burdekin M. "Rapid Volumetric Calibration of Coordinate Measuring Machines Using a Hole Bar Artefact." Proceedings of the Institution of Mechanical Engineers, Part B: Journal of Engineering Manufacture 216.8 (2002): 1083-1093

4. Ludicke, O. "Novel Multi-wave Standards for Calibration of Form Measurement Instruments." Proc. 1st EuSPEN, Bremen, 2 (1999): 299-302
5. Phillips, S., et. al. "A Novel Artifact for Testing Large Coordinate Measuring Machines." Precision Engineering 25.1 (2001): 29-34
6. Savio, E., De Chiffre, L. "An Artifact for Traceable Measurements on Coordinate Measuring Machines." Precision Engineering 26.1 (2002): 58-68

4 ULTRAFORM 2D

Alex Sohn
Ken Garrard
PEC Staff
Thomas A. Dow
Professor
Department of Mechanical and Aerospace Engineering

4.1 INTRODUCTION

Profilometers for performing form and roughness measurements have traditionally been based on cartesian geometry. Measuring parts with large aspect ratios presents a significant challenge for commercially available measurement systems. Optical profilometers are slope limited to a few degrees by the ratio of fringe spacing to camera resolution. Mechanical profilometers are usually limited by the clearance angle of the tip and the non-perpendicular loading direction of the probe – both of which often limit the measurable slopes to less than 45°. Certain industries, those making high aspect-ratio optics in particular, require the measurement of geometries more polar than cartesian in nature. A polar profilometer, called *Polaris*, was designed and built in 2000 at the PEC to address this need [1, 2]. The device is capable of measuring figure as well as roughness on hemispheres and aspheres both concave and convex inside a circular measurement field 50 mm in diameter. This design can be used to measure surfaces to a resolution of 20 nm and an overall accuracy of 200 nm.

Ultraform 2D, shown in Figure 1, is a commercial prototype of the polar profilometer *Polaris*. As a joint project with Precitech Precision, Ultraform 2D maintains the layout and concept of *Polaris* while certain components have been changed to make the instrument commercially viable. The most significant change to the machine is an increase in both R-axis travel as well as measurement range. The travel of the R-axis has increased to 70 mm on Ultraform while the overall measurement field has been increased to 100 mm by the addition of a manually adjustable LVDT positioner.

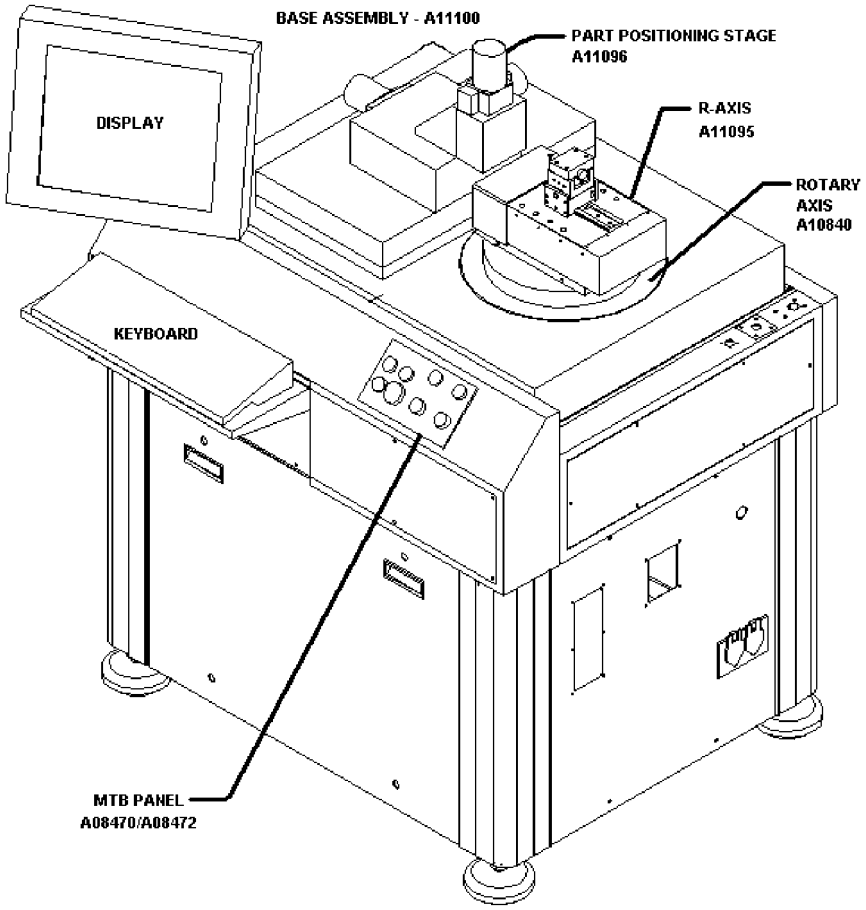

Figure 1. Drawing of Ultraform 2D

4.2 CHANGES FOR COMMERCIALIZATION

4.2.1 HARDWARE CHANGES

Several changes were made in hardware to either improve performance, reduce cost or both. Some components were not suited to a production machine whereas others that were purchased from other vendors could be produced by Precitech. A summary of components for each machine is shown in Table 1.

MAJOR COMPONENT COMPARISON		
Component	**Polaris**	**Ultraform**
Vibration Isolation	Fabreeka Precision Aire	Fabreeka Precision Aire
Machine base	Rock of Ages	Rock of Ages
Three-axis part positioner	NEAT Stepper	NEAT Stepper
Part mounting plate	Bolt Grid	Vacuum Chuck
Rotary Air Bearing	Precitech RT 200/270	Precitech RT 200/270
Rotary encoder	Heidenhain	Renishaw
Linear Air Bearing Slide	Dover	Precitech Custom
LVDT Support	Fixed	Adjustable
Air-Bearing LVDT	Lion/Colorado Precision	Precitech
Rotary Stage Motor	Aerotech Brushless, Frameless	Hathaway Brushless, Frameless
Linear Motor	Trilogy	MTS
Controller Cabinet	ElectroRack/Desk Type	Precitech Custom/In machine base
Linear scale	Heidenhain	Sony
PC	IBM NetVista	Panel PC
Motion Controller	Delta-Tau UMAC	Delta-Tau UMAC

Table 1. Hardware comparison of Ultraform 2D and Polaris

The vibration isolation system from Fabreeka performed flawlessly and exceeded all performance expectations on *Polaris*. This system was retained based on experience, reasonable cost and the importance to the isolation system. Similarly, the granite slab to provide mass for effective damping and a stable platform for the machine continues to be sourced from Rock of Ages.

The three-axis part positioner remains the same for both machines with the exception of a longer travel in the Z-direction to accommodate the longer travel of the R-axis. All three positioning axes are driven by microstepping motors to give an overall position resolution of 0.5 μm. The part mount on the positioner has been changed to accommodate a vacuum chuck in place of the grid of bolt holes of *Polaris*.

The rotary stage (θ-axis) has been modified. While the Precitech air bearing table remains the same, the rotary encoder and the motor are somewhat different. The Renishaw rotary encoder has increased the rotary axis resolution to 0.1 arcsec from the previous 1 arcsec Heidenhain encoder, mainly due to a tenfold increase in interpolation. The Hathaway rotary axis drive motor is of the same type as the previous Aerotech model, with a three-fold reduction in torque from 11.7 N-m peak to 3.8 N-m peak. It was selected mainly for space and cost saving reasons. Since the θ-axis does not need to accelerate or decelerate rapidly, this reduction in torque should have no impact on the operation of Ultraform.

The linear (R) axis has the most significant changes. *Polaris* used a Dover box-slide design of anodized aluminum with encoder and motor on either side outboard of the slide. Precitech has designed a new dovetail slide with 70 mm of travel that is based on aluminum dovetail slides used in some Optoform diamond turning machines. Shown in section in Figure 2, the slide is constructed of stainless steel and accommodates both the linear motor and encoder in the center of the dovetail. This eliminates the Abbé offset in the tangential direction present on the Dover slide that contributes to yaw errors. The motor on Ultraform is an MTS model with 43 N peak force as opposed to *Polaris's* Trilogy model with 133.5 N peak force. Due to space constraints, the coil size was reduced along with the force. The Heidenhain Diadur linear scale with 20 nm resolution has been upgraded to a Sony scale with 10 nm resolution.

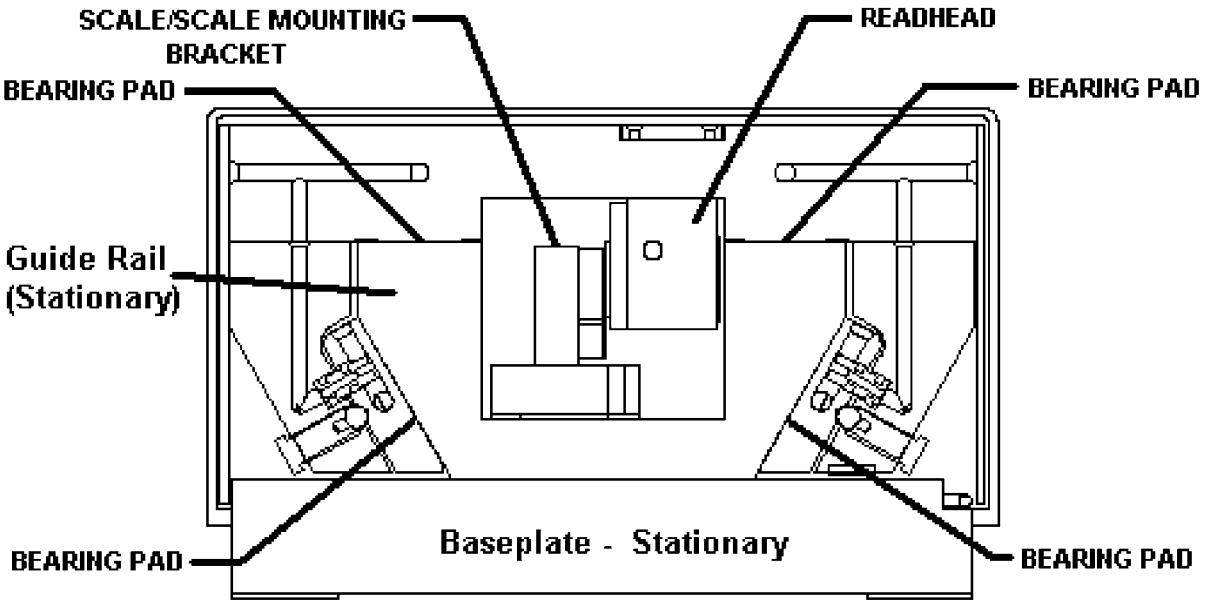

Figure 2. Cross section of linear air bearing slide. Note the dovetail shape and center mounted linear scale. The linear motor resides immediately behind the scale.

Significant changes have been made to the mounting for the air-bearing LVDT gauge. Adjusting the position of the gauge for probe centering on *Polaris* required tapping the monolithic mount. Ultraform has a fully adjustable base as shown in Figure 3. A differential thread screw allows fine adjustments of the LVDT's tangential position. Additionally, the bottom of the mount is dovetailed to allow the LVDT to be positioned manually in the R-direction, increasing the coverage area for measurements to a 100 mm diameter circle.

The arrangement of the control system has been changed as well by placing all components on a single machine base. *Polaris* had a separate desk, which contained all of the control components, provided workspace and accommodations for the PC. In place of the desk,

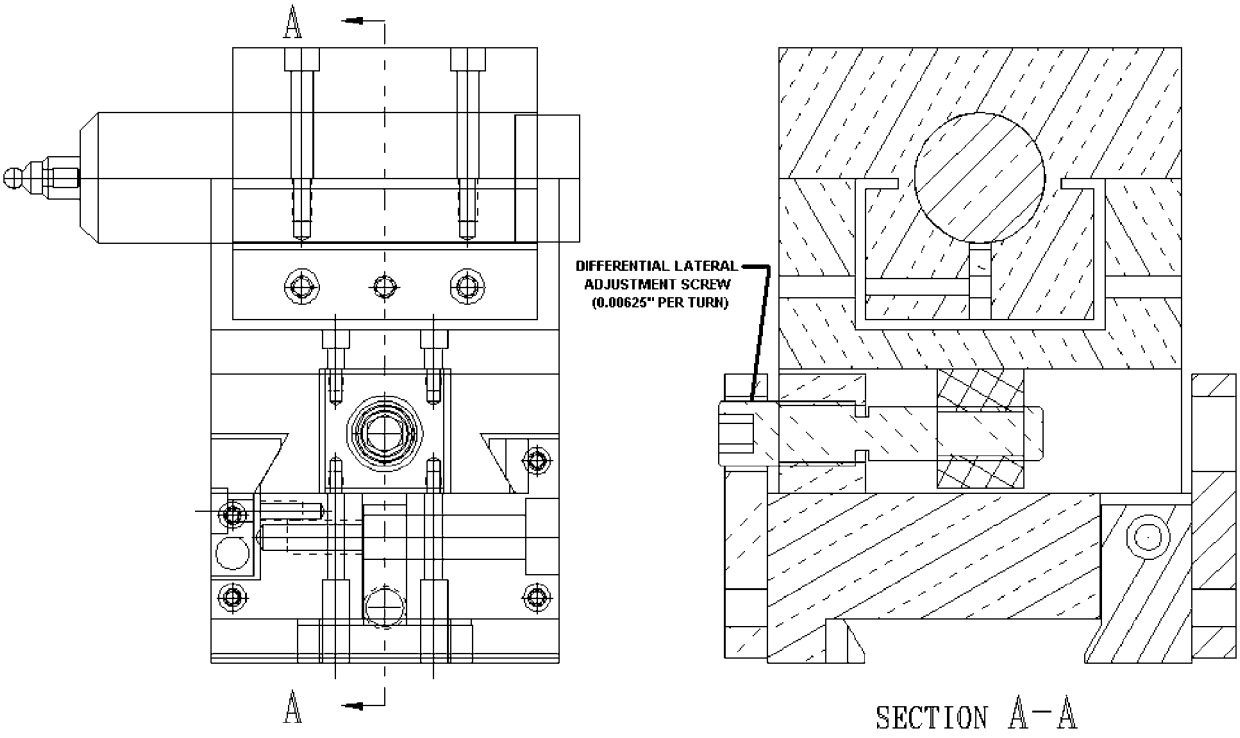

Figure 3. The LVDT holder is now adjustable with differental screw horizontally perpendicular to the LVDT axis. The mount also slides on a dovetail mounted to the R-axis to allow a larger measurement envelope.

Ultraform uses a panel PC mounted on a stalk on the side of the machine. The Delta Tau UMAC motion controller Is the same as on the *Polaris*. While hardware has not changed, software changes are significant.

4.2.2 SOFTWARE MIGRATION

Migration of the *Polaris* software to the Ultraform platform will require significant modifications to code at three different levels. At the lowest level is the Delta Tau firmware and the data structures that configure it to control the hardware. Included in this category is the 512K x 24-bit data acquisition buffer. The next level includes the software PLCs and motion programs that implement the operational functions required to setup, perform axes calibration and measure a specimen. The top level is the User Interface (UI) software that executes on a PC host computer connected to the UMAC controller via USB. With the exception of the handwheel jogger, the mounting of a specimen on the 3-axis part positioner and the power on/off, emergency-stop and emergency-stop reset switches, all user interactions with the machine are through the UI program. Communication among the software components is through global access to the UMAC's internal variables and the acquisition buffer. The division of operational tasks among the UI, control PLCs and motion programs is the principal update required of the prototype software.

Performance Improvements

Crowning and Calibration Several operational tasks in the Polaris need to be improved. The auto-crowning and calibration procedures can occur faster if the process of nulling the probe against a part is performed by a triggered jog procedure (PLC or motion program) on the UMAC instead of by incremental jog and test loops on the host PC. Probe nulling is performed by moving the Z axis during crowing, the R axis during calibration and both R and Z when initiating a measurement.

Data Acquisition The time to uploading data after completion of a measurement can be reduced by utilizing the PMAC library routines for transfer of binary data. Presently the data is "dumped" to the host PC in ASCII format and converted to a numeric format for analysis. The conversion process is insignificant, but transferring the data as characters requires about twice the USB bandwidth. Also, the USB channel incurs significant setup overhead for each communication cycle relative to its ultimate per byte transfer rate. Thus a large data transfer buffer is desirable.

Data Analysis Two types of least-squares curve fitting are implemented by the UI software: linear (slope and intercept) and circular (radius and center coordinates). Both are performed on the data after it is converted to Cartesian coordinates. This transformation of the data leads to uncertainty in both the independent variable (the abscissa or X axis) and the dependent variable (the ordinate or Z axis). In addition, the required least-squares assumptions of independence and Gaussian error distributions are violated as a result of the transformation. The technique used for the circular fit is known to be very susceptible to round-off errors and to fail completely in some

trivial, degenerate cases (e.g., when the data forms a vertical, straight line). The preferred algorithm for general linear least-squares is known as the Singular Value Decomposition (SVD). Either the SVD or a general purpose non-linear algorithm (e.g., Levenberg-Marquardt) will be used for all curve fitting. It may also be possible to implement the fitting routines with the polar coordinate data to avoid the problems associated with the transformation.

Control

The machine control software is logically divided into two categories: PLCs and motion programs. PLC's control essential functions such as emergency stop, jogging and homing. Motion programs are used for activities that require both synchronized motion along a prescribed path and data acquisition. The final (ρ, τ) calibration step, θ calibration and part measurement are done with motion programs. The calibration motion programs are stored in the UMAC's non-volatile program memory. Coarse (ρ, τ) calibration and X,Y crowning were performed by the UI issuing jog commands directly to the UMAC and waiting for motion to complete. These functions will be improved with saved motion programs to simplify the UI interactions with the control system. Improved performance is also expected.

LVDT Following Mode For *Polaris*, a new part measurement motion program that drives the R and θ axes along a nominal part profile was generated by the UI software and downloaded to the UMAC for each measurement setup. For Ultraform, a more generic measurement mode will be implemented that does not require a nominal probe trajectory. Techniques for using the LVDT signal as a secondary feedback for the R axis motion control are being investigated. This will eliminate the need for generating nominal part profile motion programs and measurement offsets and permit the measurement of surfaces of unknown cross-section. It may still be desirable for the user to specify whether the part is concave or convex at its apex although this information may be available from the crowning procedure. During measurement of an unknown surface, the θ axis will be commanded to rotate slowly through a prescribed arc length while the controller maintains a null LVDT feedback signal by moving the R axis in response to displacements of the probe. Four approaches for implementing LVDT following mode have been identified.

1. **Periodic modification of the commanded position for the R axis.** A test was performed with the prototype instrument using a simple motion program. In this test, the R motor was defined as the W axis in a coordinate system and commanded to follow an appropriately scaled LVDT feedback signal. Rotary table motion via incremental jog commands was generated by the handwheel jog PLC. The trade-off between delay timing and motion velocity was found to be critical as the R axis has a high bandwidth (~50 Hz) and can "bounce" the probe. The resulting instability would be a major obstacle to measuring parts with large local slopes.

2. **Dual feedback.** That is, the controller uses a linear combination of the LVDT signal and the R axis encoder signal as the control feedback for the R axis. The UMAC firmware allows for both position and velocity feedback as well as master-slave following modes. A typical example is the slaving of an axis to a manually operated handwheel or a spindle.

3. **LVDT-only feedback for the R axis.** A significant problem occurs if the probe looses contact with the surface during measurement. Switching between feedback signals is also problematic.

4. **The inverse kinematics** facility of the UMAC provides a means of "getting inside the loop" with respect to trajectory command generation. Although similar to the dual feedback technique, the inverse kinematic PLC is executed on every servo cycle (currently fixed at 440 μsec). The constant timing simplifies the task of implementing a low pass filter to avoid problems associated with the low bandwidth, directionally dependent response the LVDT air bearing.

With all four techniques, two issues must be resolved. First, rapid corrective motions of the R axis must be filtered or the air bearing LVDT will loose contact with the surface; second, the transition into and out of following mode must be smooth.

Triggered Moves To move a specimen into contact with the LVDT probe, two triggered jog motion programs will be implemented. One will move the R axis (calibration operations and measurement setup) and the other will move the Z axis (X and Y axis crowning). Currently these operations are performed by the UI as a sequence of discrete UMAC commands: *move*, *wait for motion to complete* and *check LVDT position and status*. The sequence is repeated until the LVDT signal is sufficiently close to zero. Finding the part with the probe can be time consuming as the R or Z axis commanded motion cannot exceed the range of the LVDT. Thus, many iterations are required if the part and probe are not jogged close to one another by the operator before starting automatic motion command sequences (e.g., calibration, crowning, measurement). Replacing this rather tedious technique with triggered moves will represent a significant time saving for the operator.

User Interface

The user interface is a Windows application written in C and C++ using the Borland C++ Builder integrated development environment. The Delta Tau PComm32 library provides functions to communicate with the UMAC controller and the Iocomp Plot Pack and Instrument Pack component libraries provide 2D plotting facilities and instrumentation display capabilities (e.g., analog gages, LEDs, progress bars, etc.).

Data Files Three types of files are created by the UI:

1. **The Preferences file** (Polaris.ini) is a binary format file containing the user selectable preferences accessed via the **Preferences** menu and the results of the most recent calibration.
2. **Part data description files** (*.pdm) are the result of processing a G-code file to create a motion path for the UMAC axes to follow. These files will no longer be needed after the LVDT following mode is implemented.
3. **Measurement data files** (*.mdm) are the saved ASCII data acquired by the controller during a measurement scan. They consist of six columns of numbers preceded by a single header line containing column labels. The columns labels are: **Index**, **X**, **Z**, **R**, **Theta** and **Rho**. Index is simply a sequence number for the each data row, X and Z are the data points expressed in Cartesian coordinates and R, Theta and Rho are the positions of the moving axes at each data collection interval. X, Z and R are in units of millimeters, Theta is in degrees and Rho is in micrometers. The data is saved after compensation for LVDT linearity, R axis pitch, (ρ, τ) offsets and probe radius are performed. The X,Z Cartesian transformation is relative to $(X_0,Z_0)= (0,0)$. Improvements in the measurement file format are needed. In addition to column labels the header should contain the data and time of the measurement, the calibration information used to compensate the data, the LVDT range setting and the spatial filter parameters used to calculate surface normals.

Code Modules The most significant UI code change needed for the migration from *Polaris* to Ultraform is the separation of the command and control functions from the data analysis and plotting functions. *Polaris* UI software also contains numerous interaction sequences with the UMAC PLCs and motion programs. Simplification of these interactions by directing all communication activities through a single module will facilitate debugging, code maintenance and the possible future migration to different controller hardware. From experience with the *Polaris* prototype, it is also apparent that the mechanisms employed for data allocation and thread management (ie, multi-tasking) are not robust. The separation of code modules into functional groups and redesign of these features will reduce the occurrence of errors and execution speed of the code.

4.3 TESTING

Preliminary measurements have been made to characterize error motions of Ultraform 2D. Straightness measurements of the linear (R) axis revealed horizontal straightness of 160 nm and vertical straightness of 100 nm over the axis travel of 70 mm. Compensation will be performed for the horizontal straightness to achieve overall measurement accuracy of 100 nm. R-axis pitch, of particular concern due to the large Abbé offset between the linear encoder and the LVDT gauge, was measured to be 0.4 arcsec on Ultraform. This is a significant improvement over the 1 arcsec value obtained for *Polaris*. It does, however, still produce an error of 230 nm over the axis range. As in *Polaris*, this error will be compensated for in software. Finally, the θ-

axis roundness was found to vary by as much as 180 nm over the measurement range. This error will also be mapped and compensated.

4.4 PROBE WAVINESS COMPENSATION

Of significant concern for achieving an overall accuracy goal of 100 nm with Ultraform is the waviness of the probe tip. Typical carbide or ruby probe tips are available in a grade 5 (±5 μin or ±125 nm) roundness. This represents an appreciable error, which must be accounted for in each measurement. To eliminate this error, a calibration technique will be used. Each time a probe tip is placed on the machine, a flat will be measured near the θ-axis center of rotation. For a perfectly aligned probe tip with no waviness, there will be no deflection of the LVDT for the measurement. Any displacement will be a combination of misalignment and tip waviness. Since these errors manifest themselves in the same way on the measurement as the calibration(they are distinguishable only by their degree of symmetry), they need not be separated, only mapped and removed from measurement data.

4.5 CONCLUSION

The commercial prototype of Ultraform 2D is expected to be completed by October 2003. Production versions will follow with a version ported to the QNX-based UPX controller platform. The prototype will returned to the PEC and used as a development platform for the Ultraform 3D, for full 3D profilometry.

REFERENCES

1. The Polar Profilometer *Polaris*, Proceedings of the ASPE 2001 Annual Meeting, **v.25**, pp. 28-31(2001)
2. The Polar Profilometer *Polaris,* 2001 PEC Annual Report, **v. 19**, pp.1-15 (2002)

5 EXPERIMENTAL STUDY ON COOLING EFFECTS GENERATED BY PIEZOELECTRIC BIMORPH STRUCTURES

Tao Wu
Graduate Student
Paul I. Ro
Professor
Department of Mechanical and Aerospace Engineering

5.1 INTRODUCTION

This report describes the experimental results of the cooling effect generated by the vibration of various piezoelectric bimorph structures. The cooling effect is measured by the temperature drop in the heat source placed above the vibrating bimorphs. Results show that the heat transfer performance of bimorph can be intensified by the introduction of slots. It is expected that the results will be helpful in further designing miniature cooling systems of microelectronic products, such as computer processors.

5.2 METHODS

5.2.1 EXPERIMENTAL SETUP

Figure 1 shows the experimental apparatus, which consists of: a piezoelectric bimorph actuator from PIEZO Systems; Function Synthesizer to generate sinusoidal signals with certain frequency and amplitude; Power amplifier with amplification factor of 100; A commercial cartridge heater from Omega (1.25inches long, 0.25 inches in diameter, 120v, 75w) is inserted into one aluminum block (1.4inches by 1inches by 0.4inches), which is served as the heat source; Thermocouple and digital thermometer are employed to measure and record the temperature of the heat source. The gap between the bimorph structure and heat source is adjusted by four micrometer devices. In addition, the heat source along with the bimorph is put in an enclosure to minimize ambient effects.

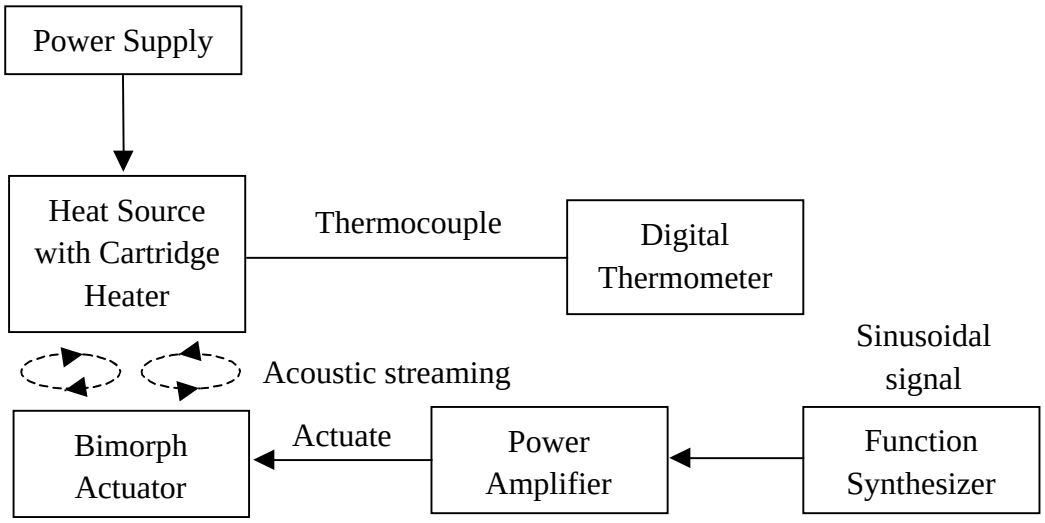

Figure 1: Experimental apparatus used to examine cooling effects of bimorph

5.2.2 BIMORPH STRUCTURES

Bimorph usually consists of two thin ceramic layers bonded together, which produces curvature when one ceramic layer expands, while the other layer contracts. A center shim (usually metals such as brass, aluminum etc.) is usually laminated between the two piezoelectric layers to increase mechanical strength and stiffness, but this reduces motion. Bimorph with one brass middle shim (PIEZO Systems) is chosen in the cooling experiments. The bimorph is 63.5mm long, 31.8mm wide and 0.191mm thick for piezoelectric layer, 0.127mm for brass layer.

In this study, the bimorph structures with and without slots are employed. Figure 2 shows the structure for bimorph with two slots and parameters. In the figure, tb and tp are thickness for the brass layer and piezoelectric batch, respectively. L is the length of the bimorph, W the width, Ls the length of the slot, Ws the width of the slot. L_edge and W_edge are the edge size in two directions.

5.2.3 PROCEDURES

The mechanism of cooling effects generated by the bimorphs is that the acoustic streaming induced by the vibration of bimorphs may enhance the convective heat transfer around the heat source. Acoustic streaming velocity is directly related to the amplitude of the vibration [1]. Hence, it is required that the excitation frequency is the resonance frequency and that can be determined theoretically [1].

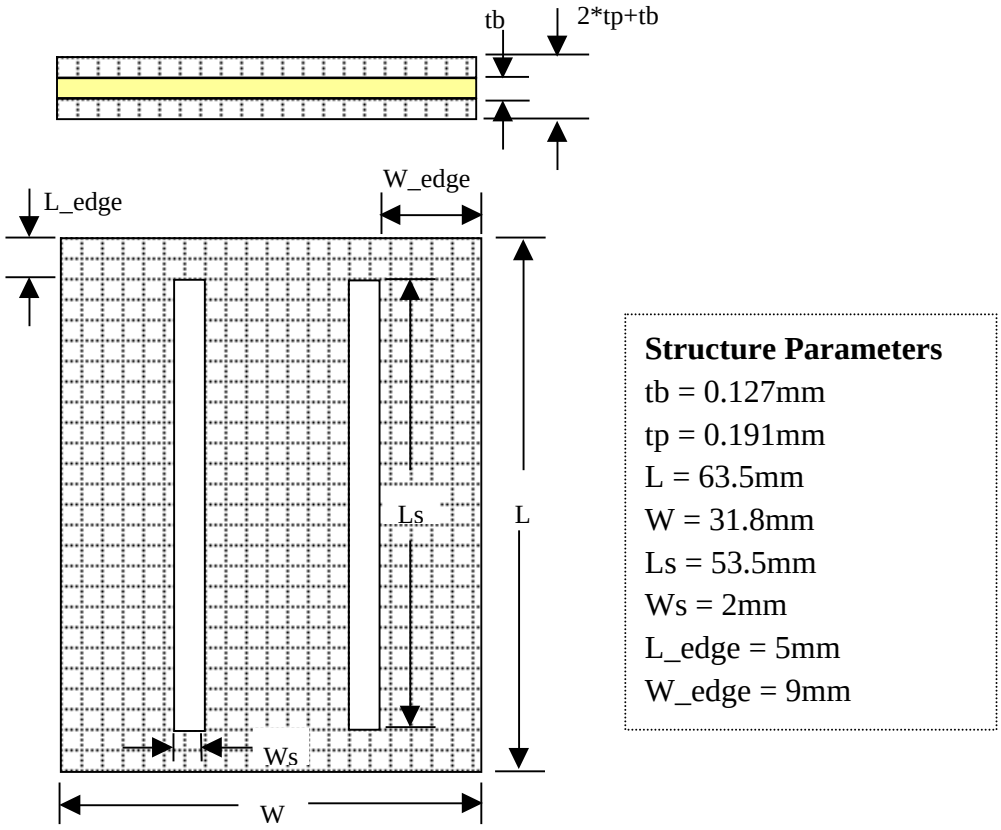

Figure 2: Structures for the bimorph with two slots

In addition, the higher the electric field to the bimorphs, the higher the vibration amplitude. However, for the piezoelectric materials, a certain limitation of electric field strength is applied. The electric field necessary to cause sufficient depolarization will create extremely undesirable operating conditions with very high dielectric losses and will result in low efficiency. The initial depolarization field of the two-layer brass reinforced bimorph used in the cooling experiments is 500v/mm.

In the experiments, the heat source is first heated to reach a steady temperature, and then two sets of data are recorded. One is recorded at five minutes after activating the bimorph. The temperature drops fast in this period, thus it is called “transient cooling process”. The other set of data are taken at the half-hour mark. After half an hour, the temperature of the heat source is nearly stable, and a steady cooling is expected.

5.3 RESULTS AND DISCUSSIONS

Table 1 and figure 3 show the variation of temperature drops in the heat source versus electric fields with the slotless bimorph. The excitation frequency is 280 Hz (fundamental resonance frequency) and the gap between the bimorph and aluminum heat source is 600μm. Clearly, with an increase in electric field intensity, the temperature drop increases first nearly linearly then tends to be saturate as the electric field closes to initial depolarization field. The maximum temperature drop under the experimental conditions is 21°C when the electric field is 450v/mm after half an hour of operation.

Table 1: Temperature Drop for Slotless Bimorph
(f = 280 Hz, Gap = 600μm)

ELECTRIC FIELD (V/MM)	TEMPERATURE DROP (°C)	
	5 minutes later	30 minutes later
250	5.4	9.7
300	7.3	12.9
350	9.3	16.4
400	11.8	20.1
450	12.2	21

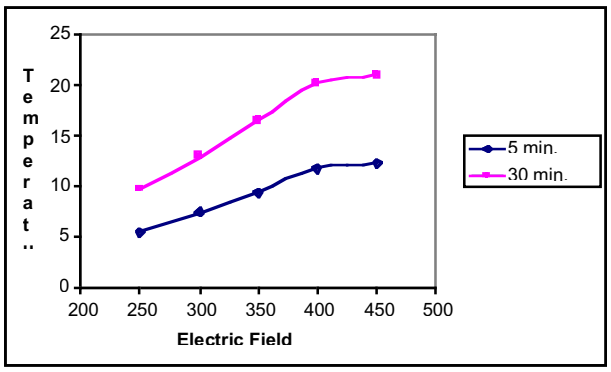

Figure 3: Temperature Drop for Slotless Bimorph

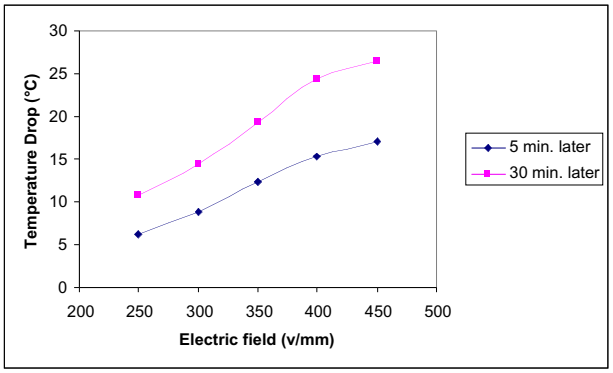

Figure 4: Temperature Drop for Bimorph with Two Slots

For the bimorph with two slots, the same aluminum heat source is utilized and the bimorph is excited at its first resonance frequency (270Hz) for comparison. The gap is kept at 600μm. Two sets of data are listed in Table 2 for 5 minutes later and 30 minutes later.

Table 2: Temperature Drop for Bimorph with Two Slots
(f = 270 Hz, Gap = 600μm)

ELECTRIC FIELD (V/MM)	TEMPERATURE DROP (°C)	
	5 minutes later	30 minutes later
250	6.2	10.8
300	8.8	14.4
350	12.3	19.3
400	15.3	24.4
450	17.1	26.4

From figure 4, it is shown that the maximum temperature drop for the bimorph with two slots is 17.1°C after 5 minutes of operation at electric field of 450v/mm and 26.4°C after half an hour. The comparison between the two bimorph structures under different electric fields can be observed in Figures 5 and 6. Two things can be observed from these two figures. One is that the vibration of bimorph with two slots gives better cooling effects [2, 3]. The other is that the temperature drop has increased by increasing the electric field.

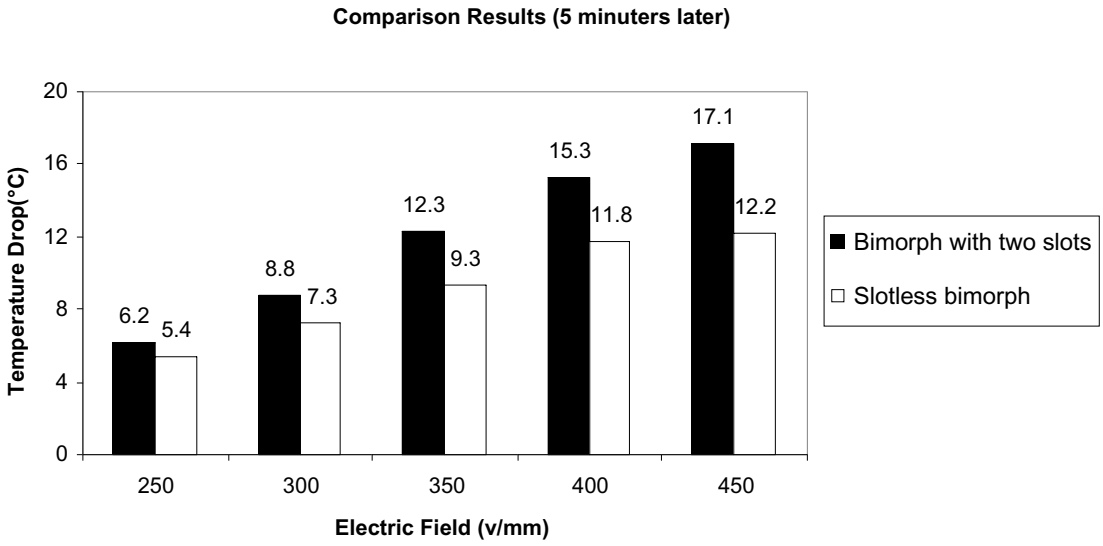

Figure 5: Comparison of temperature drop after 5 minutes

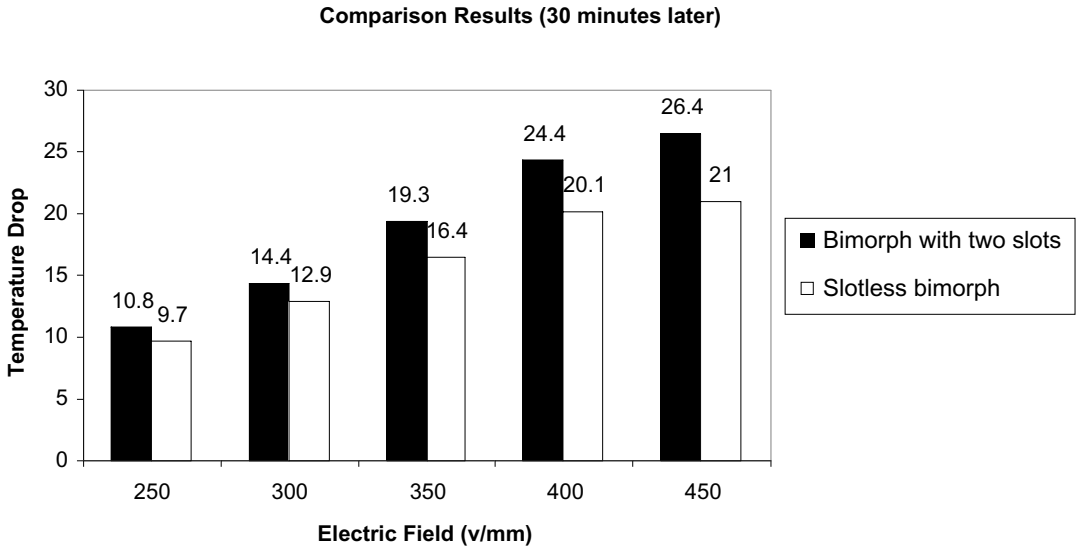

Figure 6: Comparison of temperature drop after 30

5.4 CONCLUSIONS

Experiments are conducted to compare two different bimorph geometries and empirical formulae are generated based on the experimental data. The results show that:

(1) By introducing slots to the bimorph, the cooling effects can be improved significantly;

(2) The temperature drop between the slotless bimorph and bimorph with two slots is increased with increasing electric field.

REFERENCES

1. Wu, T., Ro, P.I., Kingon, A.I. and Mulling, J.F., "Piezoelectric resonating structures for microelectronic cooling", *Smart Materials and Structures*, 12: 181-187, 2003
2. Torii, S. and Yang, W.J., "Thermal Transport Phenomena over a Slot-perforated Flat Surface in Pulsating Free Stream", *Int. J. Therm. Sci*., 41: 241-252, 2002
3. Kim, S.H. and Anand, N.K., "Use of slots to enhance enforced convective cooling between channels with surface-mounted heat sources", *Numerical Heat Transfer*, 38:1-21, 2000

6 FORCE FEEDBACK CONTROL OF TOOL DEFLECTION IN MINIATURE BALL END MILLING

David W. Hood
Graduate Student
G.D. Buckner
Assistant Professor, Mechanical and Aerospace Engineering

6.1 BACKGROUND

Injection molding is an important manufacturing process for optical and mechanical components. The hard steel dies used in this process play a direct role in the quality of molded parts. Traditionally, fabricating these dies involved rough milling followed by heat treatment, grinding, and polishing to the desired shape. Recently, high-speed machining of heat-treated steel (hardness > 55 R_c) has become a viable approach for reducing fabrication times while retaining the necessary shape control. However, as feature sizes drop below 1 mm with dimensional tolerances on the order of 10 μm, tool deflection can create significant errors in the shape of mold surfaces. Deflections associated with miniature ball end tools can exceed 30 μm, rendering finished dies out of tolerance.

6.2 TOOL STIFFNESS AND DEFLECTION

The long shank, ball end milling tools used are 0.8 mm in diameter, 4 mm long with a ball end. When used to fabricate free-form surfaces, the tool can be loaded in the axial direction, the radial direction, or both. The tool stiffness is significantly lower in the radial direction (98 KN/m) then the axial direction (1,420 KN/m), therefore regions of a machined surface where the tool is loaded primarily in the radial direction will be subject to large tool deflections and form errors. For arbitrary cutting conditions, the tool stiffness in the direction orthogonal to the workpiece (normal tool stiffness k_n) can be determined by the expression:

$$\frac{F_n}{\delta_n} = k_n = \frac{1}{\left(\frac{\cos^2 \phi}{k_a} + \frac{\sin^2 \phi}{k_r} \right)} \tag{1}$$

where ϕ is tool tilt angle, k_a and k_r are the axial and radial stiffness of the tool.

6.3 CLOSED-LOOP COMPENSATION OF TOOL DEFLECTION

Real-time force feedback can be used to predict and compensate for tool deflection during milling operations, reducing susceptibility to uncertainties in the model parameters and workpiece alignment. Two specific force feedback approaches are presented here: cutting depth prediction (based on a non-dynamic cutting force model) and tool deflection prediction (using a non-dynamic model of tool stiffness). Figure 1 illustrates the effect that tool deflection has on a groove profile. The tool tip is programmed to follow a desired path; however, due to deflection the tool tip, the tool actually creates a depth of cut less than desired (labeled "actual depth"). The shaded area in this figure represents material not removed due to tool deflection.

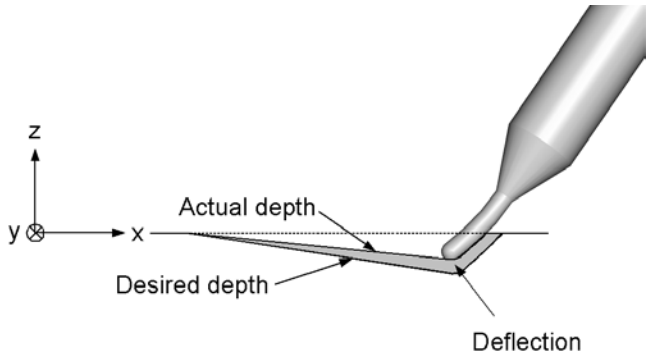

Figure 1. Tool deflection with desired and actual depth

6.3.1 CUTTING DEPTH PREDICTION

Figure 2 shows a block diagram for the cutting depth prediction control algorithm. The concept behind this algorithm is straightforward: start with a desired tool path, measure real-time cutting force, use cutting conditions and a non-dynamic force model to predict the instantaneous depth of cut, and then calculate an error equal to desired depth minus predicted depth. The error calculated by the PID control algorithm is:

$$error = desired\ depth - predicted\ depth \quad (1)$$

Once this error is known a motion program either holds the z-axis position (depth of cut), advances the z-axis into the part, or reduces the z-axis position.

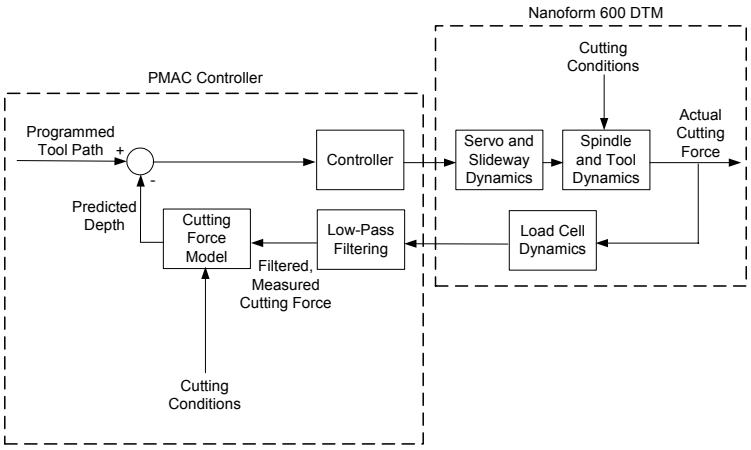

Figure 2. Diagram of predicted depth algorithm

Using the validated cutting force model, cutting depth can accurately be predicted based on cutting conditions. This predicted cutting depth is a function of the cutting force model that includes model cutting parameters. In this way the system can correct for errors associated with tool deflection and misalignment of the workpiece.

6.4 PREDICTED DEPTH COMPENSATION

To evaluate the effectiveness of the force feedback deflection compensation algorithms, machining experiments were conducted on the Nanoform 600 DTM. Groove profiles were machined in S-7 tool steel samples mounted to the three-axis load cell. The workpiece was aligned with the axes of the Nanoform and cuts were made along the x-axis (left to right) with the tool tilted at 25 degrees from the z-axis to emphasize the effects of tool deflection. Slotting cuts with linearly varying depth were made with and without compensation to evaluate the performance of real-time deflection compensation. Slots spanning 20 mm and 0-80 μm in depth were programmed, using a spindle speed of 10,000 rpm and a feed rate of 100 mm/min. This feedrate was chosen to give a chip load of 5 μm/flute.

Typical results for closed-loop compensation using predicted cutting depth and a non-dynamic cutting force model are shown in Figure 2. The upper plot represents the uncompensated cutting profile, the middle plot representing the compensated profile, and the lower plot representing the desired profile.

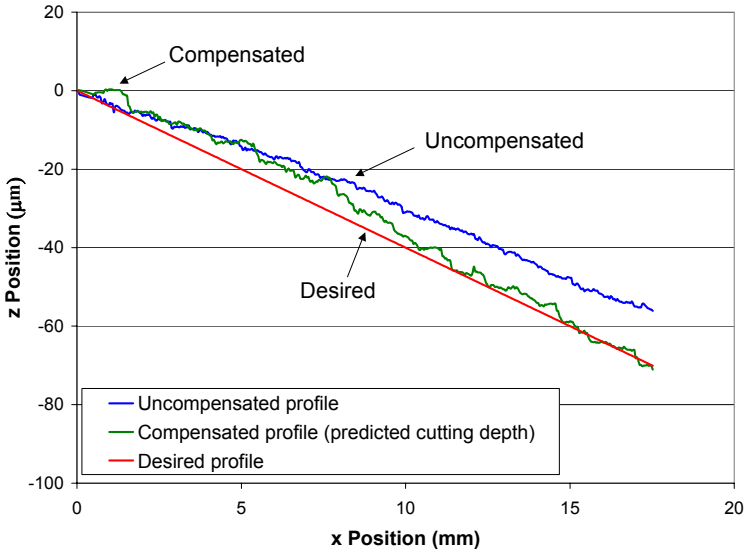

Figure 2. Experimental profile measurements: predicted depth compensation, linear slotting cut

Profile errors were not significantly improved at the start of the groove, as both the compensated and uncompensated cases reveal similar errors (approximately 0-6 µm) for the first 8 mm of cutting. From this point forward, however, predicted depth compensation significantly reduced profile errors and produced more desirable results. Maximum error in the compensated groove is on the order of 8 µm (at a horizontal location of 8 mm), while maximum error (deflection) in the uncompensated groove reaches a maximum of 14 µm at a location of 18 mm. This equates to a 43% reduction in groove profile error using the feedback scheme.

There are several reasons for this lack of error reduction at the start of the groove. One involves implementation issues associated with the DTM. When transitioning from encoder feedback to force feedback, measurable force needs to exist for cutting depth prediction to prevent a tool crash into the workpiece. Therefore, this method of compensation must be implemented after the tool begins to impart a force on the workpiece. A rotating tool is incremented toward the workpiece until a small force (on the order of 0.1 N) is measured. The axes are disabled and the mode of machine axes control is changed from encoder feedback to depth prediction compensation (force feedback). The axes are enabled, and the experiment begins. Initially, the desired cutting depth is zero. However, there is a measurable force, thus the predicted cutting depth is greater than zero. As a result, the control algorithm commands an initial move away from the workpiece, resulting in significant profile errors at the start of the groove.

Another source of error in the compensated profile involves the theoretical cutting depth vs. normal cutting force relationship. This plot reveals a very small slope at small cutting depths, making it difficult to measure forces at this operating condition due to their intermittent behavior. Thus, a small change in depth has a large effect on the force and limits effectiveness

of this method. As the depth increases, the forces become more consistent and the depth predictions become more accurate.

6.4.1 TOOL DEFLECTION PREDICTION

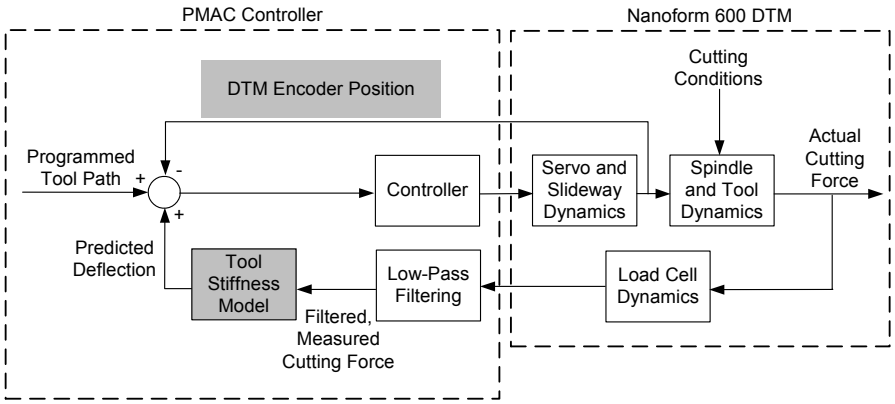

Figure 3. Diagram of predicted deflection algorithm

A block diagram of the control algorithm predicting deflection using a model of tool stiffness is shown in Figure 3. The concept behind this algorithm is straightforward: start with a desired tool path, measure real-time cutting force, use the tool stiffness model to predict tool deflection, calculate an error equal to desired position minus DTM encoder position plus predicted deflection. Once this error has been calculated, the controller either holds position, moves the z-axis toward the workpiece to increase the depth of cut, or moves away from the workpiece decreasing the depth of cut. With a validated stiffness model, deflection can accurately be predicted based on the measured cutting force. In this way the system uses real-time force feedback to correct for errors associated with tool deflection but does not depend on the predicted force model. Error calculated by the PID control algorithm is:

$$error = desired\ tool\ position - encoder\ axis\ position + \frac{F}{k} \tag{2}$$

6.4.2 PREDICTED DEFLECTION COMPENSATION

The predicted deflection compensation method was compared to uncompensated machining. A typical set of results is shown in Figure 4 with the upper plot representing the uncompensated cutting profile, the middle plot representing the compensated profile, and the lower plot representing the desired profile.

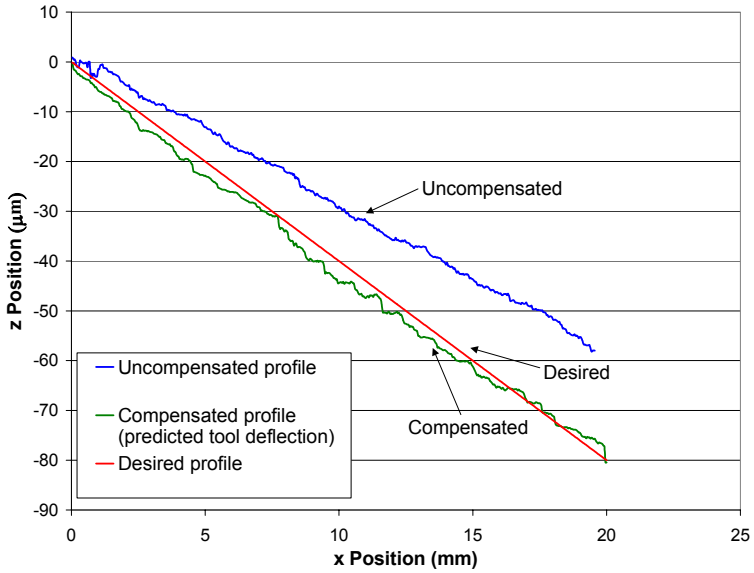

Figure 4. Experimental profile measurements: predicted deflection compensation

Normal cutting force during a typical linear slotting cut is shown in Figure 5. This cutting force data shows unfiltered force as well as "maximum force" and "filtered maximum force", which result from signal processing of the raw data. Profile errors were significantly and consistently improved throughout the cutting experiment. Maximum profile errors with predicted deflection compensation are approximately 4 µm, compared to 21 µm with the uncompensated cut. This equates to an 80% reduction in groove profile error. In contrast to the predicted depth compensation, errors are initially small and remain small throughout the experiment (between +4 µm and 0 µm), resulting in depth error at the end of the groove of -2 µm.

6.4.3 Additional Cutting Experiments

Slotting cuts with harmonically varying depth were also made with and without predicted deflection compensation to evaluate the performance of this approach. In all cases, profile errors were significantly and consistently improved with force feedback control. Repeatability experiments confirmed the consistency of these performance benefits from one tool to the next. Additionally, to verify that predicted deflection compensation is effective for more general machining, more comprehensive "large groove" experiments were conducted. The goal of these experiments was to create surfaces in which the cutting forces on the ball end mill vary in direction and magnitude during machining. These experiments also investigated the effects of forces that act in the plane of the workpiece surface. These "large groove" experiments involved fabricating a 0.5 mm deep groove in a test specimen using a 3.0 mm ball end mill and enlarging the groove by 100 µm using a 0.8 mm ball end mill. Experimental results revealed peak error

reductions from 63 µm in the uncompensated case to 18 µm using force feedback compensation, a 71% improvement. These additional cutting experiments will be summarized in the PEC Annual report for 2003.

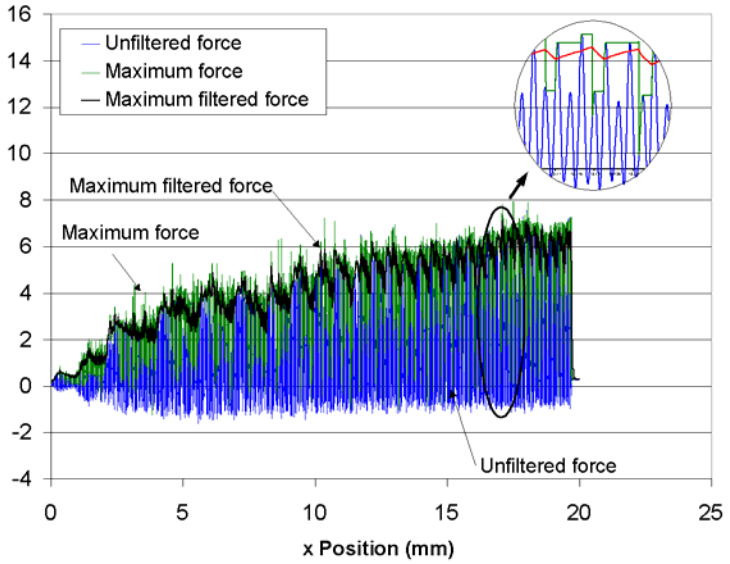

Figure 5. Experimental force measurements: predicted deflection compensation, linear slot cut

6.5 CONCLUSION

The forces generated during milling with a long, miniature ball end tool are relatively small (less than 30N) because of the limited size and strength of the tool edge. However, tool deflections can be a significant source of profile error because of low radial stiffness. Two force feedback approaches to tool deflection compensation were studied: force compensation and deflection compensation. Reduction in error in small groove profiles over non-compensated groove profiles can be as great as 80% depending on the profile and method of compensation. The success of force feedback compensation depends heavily on the acquisition, processing, and filtering of cutting forces during machining. These compensation algorithms provide an avenue to reduce fabrication times and improve surface accuracy for hardened steel mold dies.

7 CLOSED LOOP CONTROL OF TOOL DEFLECTION

Stuart Clayton
Graduate Student
Thomas A. Dow
Professor, Mechanical and Aerospace Engineering

7.1 INTRODUCTION

Milling with small diameter cutters can produce errors in the shape of features machined on hard materials. Typically the small diameter is needed to reach down into complex features and the large difference between the radial and axial stiffness of the tool will create form errors in the part. The goal of the research discussed here is to find an automatic way to compensate for these errors and improve the quality of the machined components.

While the open loop deflection compensation algorithm requires the cutting force model, the closed loop technique involves deflection compensation based on measured force. There are two major quantities that must be known, force and stiffness. The idea is to measure the cutting force in real-time, predict a deflection based on the stiffness measurements and compensate with the piezoelectric (PZT) actuator on the spindle. Two methods of measuring force were explored. The first method involved measuring the Z-component of the machining forces on the workpiece and the second method involved measuring the axial component of the tool force on the spindle.

Figure 1 shows the orientation of the spindle with respect to the workpiece. Notice the axial spindle force (Y'-direction) is equivalent to the Z-workpiece force times the cosine of the tilt angle, α. The spindle is mounted on the slide of the DTM and can move in the z-direction. Tool deflection occurs in both the Y' and Z' directions, while the PZT actuator can only move in the Z' direction. However, both directions of deflection can be compensated, because the tool tilt angle is known, as will be discussed later.

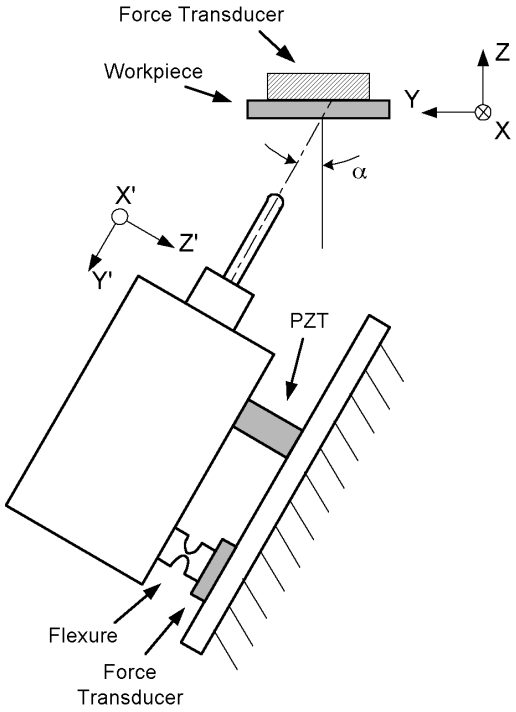

Figure 1. PZT-Actuated Spindle Orientation

7.2 FORCE MEASUREMENT ON WORKPIECE

7.2.1 CONTROL ALGORITHM

Equation (1) is the control algorithm used with this technique. It shows how the force measurement is turned into a position error using the tool stiffness. The "desired position" for the spindle mounted error compensation technique is zero. So for the error in Equation (1) to be zero, the tool deflection (force/stiffness) must be compensated by PZT motion. The result is a tool that appears rigid and errors from tool deflection are eliminated from the part.

$$error = position_{desired} - position_{actual} + \frac{force}{stiffness} \tag{1}$$

A block diagram of the control scheme can be found in Figure 2. The inner loop of the block diagram reflects the feedback from the capacitance gage used as position feedback from the PZT actuators. The capacitance gage signal was scaled to provide feedback of the displacement of the tool tip. The outer loop reflects the measured force transformed to estimate total tool deflection.

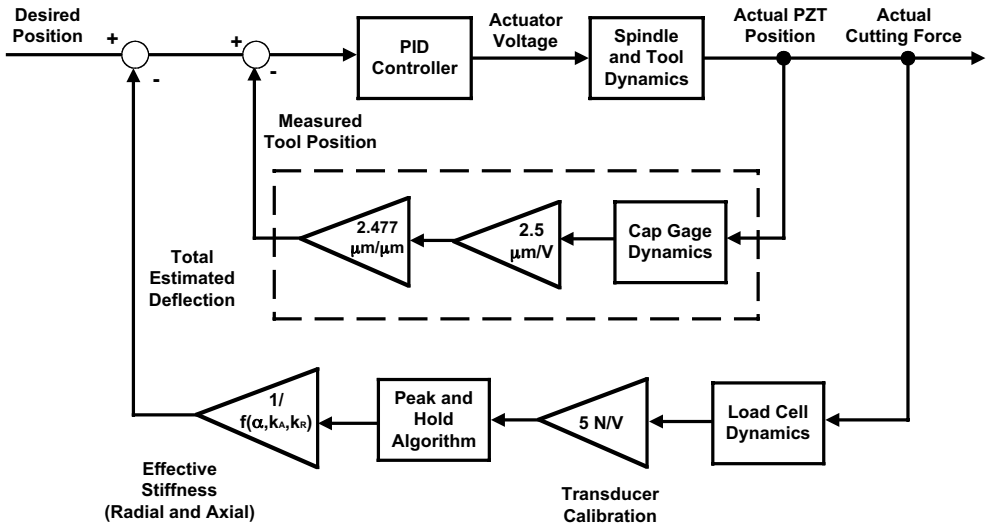

Figure 2. Block Diagram for Workpiece Feedback Control

Both radial and axial components of tool deflection can be compensated by motion of the PZT actuator on the spindle. Figure 3 shows the tool and the components of the workpiece force (F_z) broken into components normal to ($F_{z'}$) and along ($F_{y'}$) the spindle. It also shows the deflection in the Z' and Y' directions and δ_{PZT} - the scaled PZT deflection needed to correct the tool deflection normal to the workpiece. An expression for the PZT deflection needed to correct the tool deflection as a function of the force, stiffness and deflection is given in Equation (2).

$$\delta_{PZT} = \frac{F_Z \left[\frac{\sin^2 \alpha}{k_R} + \frac{\cos^2 \alpha}{k_A} \right]}{\sin \alpha} \tag{2}$$

7.2.2 EXPERIMENTAL RESULTS

Experimental tests were conducted on S7 steel with a spindle speed of 10,000 rpm. The desired groove profile consists of a linearly varying depth from 0-80 μm over a length of 20 mm. Figure 3 is a plot of raw z-force from the workpiece force transducer captured during a 20° tool tilt experiment. Note that the force does not smoothly increase as expected with the linear increase in depth of cut. A peak and hold algorithm with reset was implemented to extract the peak force for each tool rotation. Based on this force, an effective radial deflection was calculated at each time step based on tool tilt, stiffness, and current tool force. This value was used in the control algorithm, Equation (1), to generate a new voltage command to the PZT. A plot of the calculated effective radial deflection based on the maximum, filtered z-force is shown in Figure 4. Notice the maximum radial deflection (δ_{PZT}) is approximately 40 μm. This corresponds to a Z-direction error on the part of 15 μm.

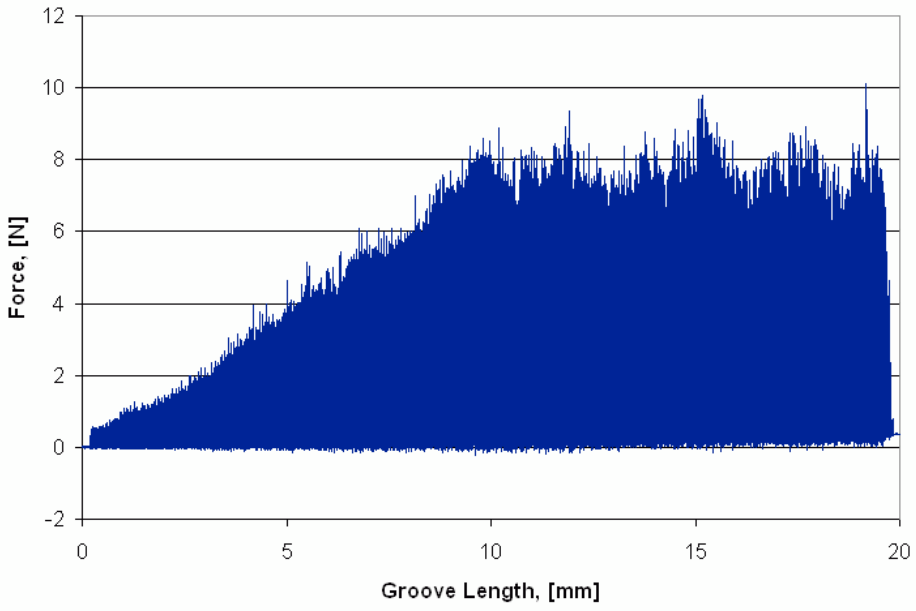

Figure 3. Raw Z Force from 20° Tilt Closed Loop Experiment; Depth = 0-80 μm, Upfeed = 10 μm/rev, Spindle Speed = 10,000 rpm, 4 mm long tool shank

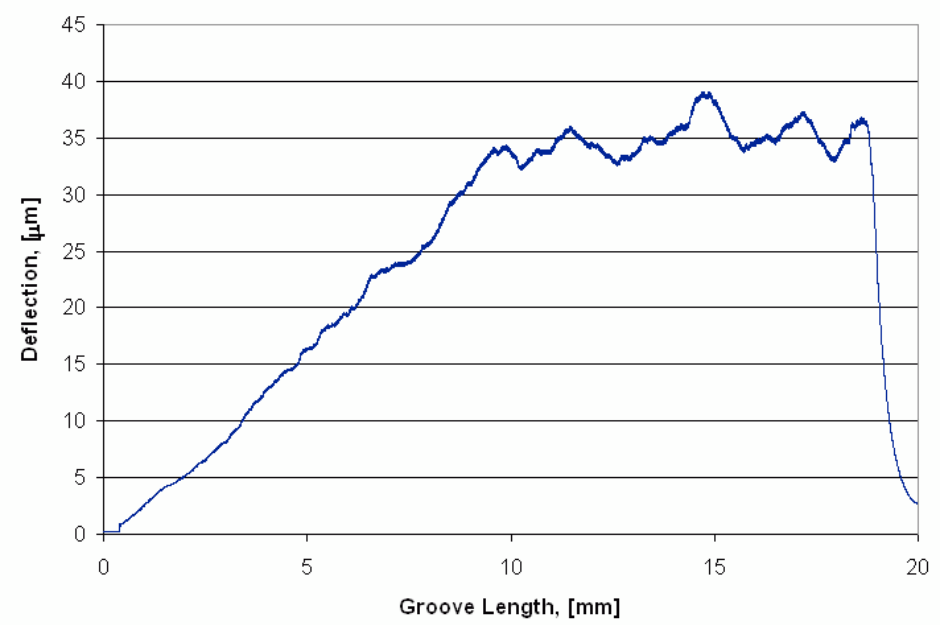

Figure 4. Effective Radial Deflection from 20° Tilt Closed Loop Experiment; Depth = 0-80 µm, Upfeed = 10 µm/rev, Spindle Speed = 10,000 rpm, 4 mm long tool shank

Groove profiles measured by the Talysurf profilometer (Figure 5) illustrate the improvement in fidelity of the groove for the closed loop compensation when compared with no compensation. Both cuts were made with "long" (4 mm shank) with a 5-µm wearland. Without compensation the error is on the order of 12 μm and this becomes less than 4 μm with compensation.

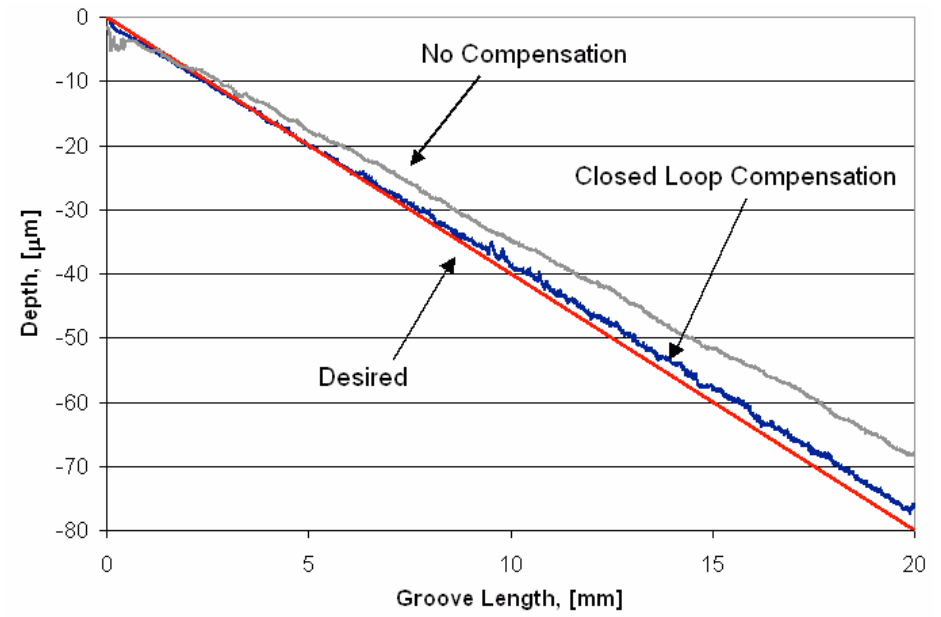

Figure 5. Closed Loop and No Compensation Groove Profiles from 20° Tilt Experiment; Depth = 0-80 µm, Upfeed = 10 µm/rev, Spindle Speed = 10,000 rpm, 4 mm long tool shank

Results from 20º tool tilt experiments show that force feedback deflection compensation using the spindle PZT has been effective and shape errors were reduced by (65%). The limit for creating the desired shape can have a variety of sources. The feedback control system did an excellent job keeping the error in Equation (1) less than 500 nm. As a result, the accuracy of the groove shape will be a function of uncertainty in 1) measurement of the groove, 2) force measurement, 3) transducer calibration, 4) tool stiffness measurement and 4) the touch off procedure used to find the part and begin the experiment.

The groove shape is measured by dragging a Talysurf probe down the center of the groove with the overall depth dependent on leveling the trace with the start and end points. The test pieces are ground flat so the surface of the part is assumed to be straight between the start and end points. To evaluate the validity of this assumption, the measured normal force and shape of an uncompensated groove with the tool tilted at 20˚ is shown in Figure 6. Notice the depth of the groove generally (but not exactly) followed with the force over the 5-minute duration of the experiment, but that neither was linear. Since there was no force feedback and a linear increase in depth was commanded, the nonlinear force and groove shape has not been explained. It could be a result of a non-flat part, material variations, or other effects. These unknowns may limit the capability of this technique to produce a perfect part.

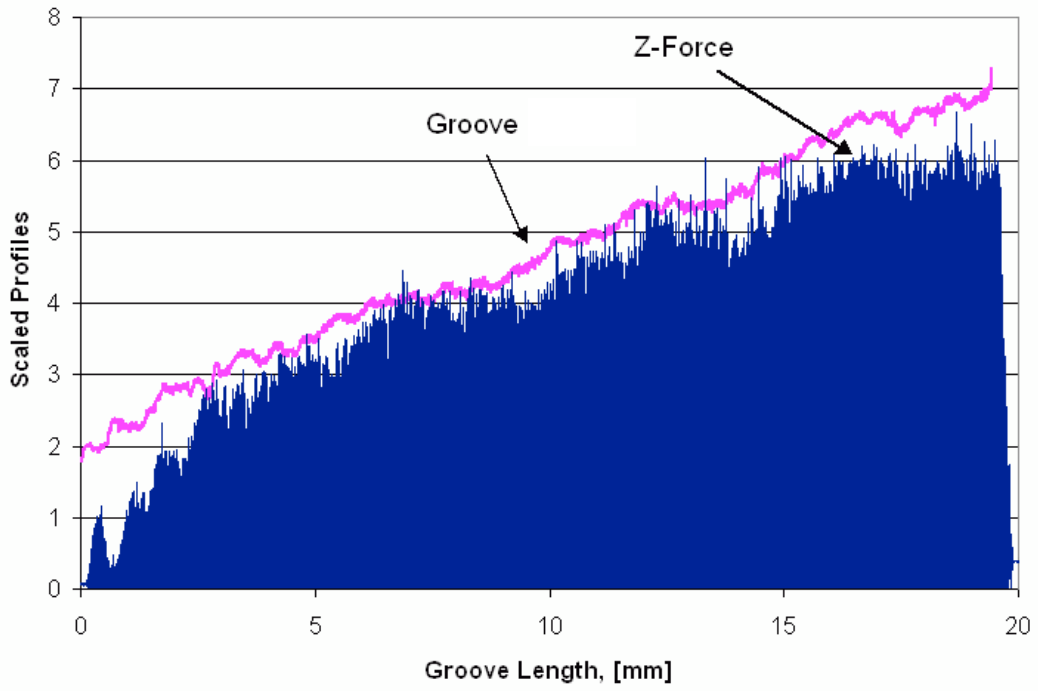

Figure 6. Force and groove profile for uncompensated 20º Tilt Experiment;
Depth = 0-80 μm, Feed = 100 mm/min, Spindle Speed = 10,000 rpm, 4 mm long tool shank

7.3 FORCE MEASUREMENT ON SPINDLE

Measuring forces on the spindle offered several advantages over measuring forces on the workpiece. One advantage is the opportunity for a self-contained apparatus that could measure forces and correct for tool deflection. This allows tool deflection algorithms to be implemented independent of workpiece properties such as size and mass. Another advantage of a self-contained design is that the force can always be measured along the radial or axial direction of the tool, without the need to know the tool tilt angle.

7.3.1 SPINDLE FORCE CALIBRATION

A three-axis force transducer of the same type used to support the workpiece was built into the spindle. However, the location of this transducer made prediction of the tool forces more complicated and a calibration procedure was employed. The relationship between forces acting on the tool tip and forces measured by the transducer was measured by applying known loads to the tool tip and recording the measured forces in each direction on the transducer. Figure 7 is a schematic illustrating the calibration technique both in the axial (A) and radial (B) directions.

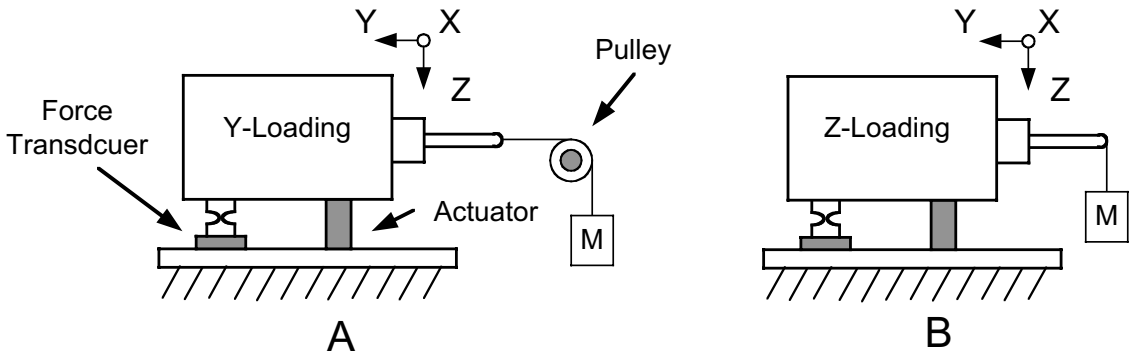

Figure 7. Schematic of Static Calibration Technique

A linear trend line was used to relate the tool-tip force to the measured transducer force in each direction. The coefficient matrix of Equation (3) was then assembled from the force ratio plots. It should be noted that the force transducer measures a coupled effect from y and z-tool forces. This was due to the moment that was applied with an axial load. In other words, an axial tool load produced both forces in the y and z-directions of the transducer.

$$\begin{bmatrix} L_x \\ L_y \\ L_z \end{bmatrix} = \begin{bmatrix} -0.50 & 0 & 0 \\ 0 & 0.44 & 0 \\ 0 & 0.80 & -1.91 \end{bmatrix} \begin{bmatrix} F_x \\ F_y \\ F_z \end{bmatrix} \tag{3}$$

The load cell to tool force transformation is given in Equation (3) where L_K refers to the measured force in the (x, y, and z directions) and the F_k represents the forces recorded in each direction on the load cell. This matrix can be inverted to find the forces applied to the tool based on the load cell readings and used for compensation. One complication of this design was cross-talk between the actuation and measurement systems. When the PZT actuators were extended, the force transducer recorded a reduction in force. This is not ideal, but repeatable measurements made it possible to produce a second calibration curve, which was added to the control algorithm to compensate for this effect.

7.3.2 CONTROL ALGORITHM

The control algorithm used with the spindle-mounted force transducer was somewhat different than the algorithm used with the workpiece transducer because of complications of the spindle force measurement. The block diagram for spindle feedback can be found in Figure 8. The major difference is the capacitance gage signal fed into the force signal to compensate for the actuation/force effects discussed above.

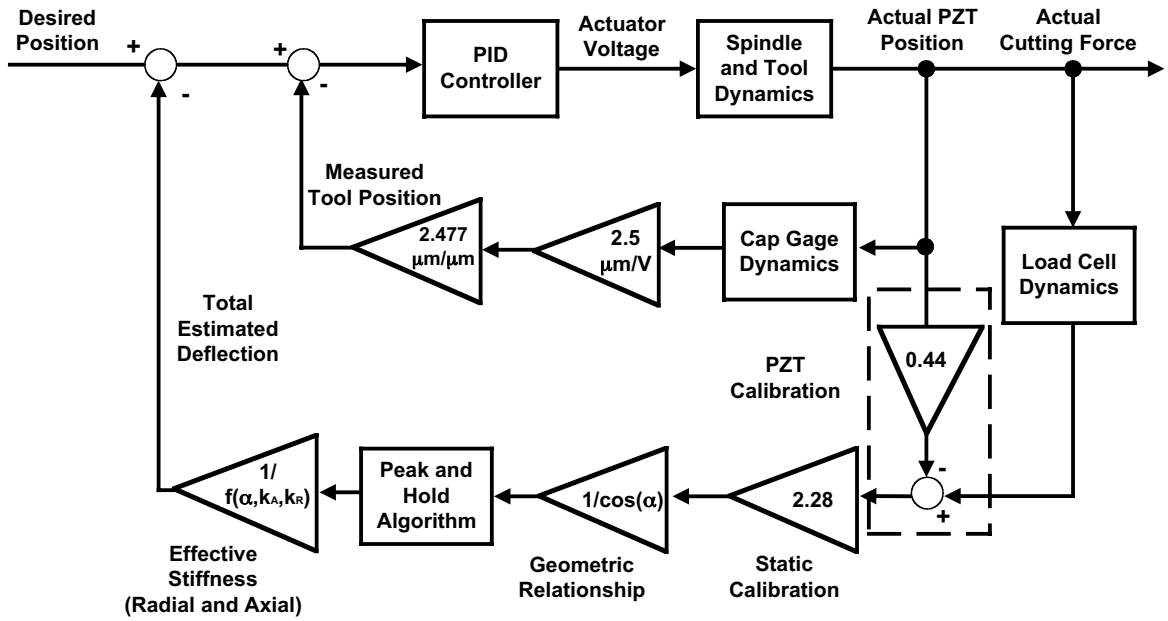

Figure 8. Block Diagram for Spindle Feedback Control; Dotted Area Implies Substantial Change from Workpiece Force Algorithm

7.3.3 EXPERIMENTAL RESULTS

Experimental cuts were made in S7 steel with 30º tool tilt using the feedback algorithm. Figure 9 shows the compensated groove with spindle force feedback as well as a groove without compensation. The groove profile compared well with the desired 0-80 μm depth over the groove span of 20 mm. Notice that the spindle feedback groove overcompensated at the start of the cut (4 μm error) but ended at the desired depth of 80 μm. Over most of the groove, the error was less than 2 μm.

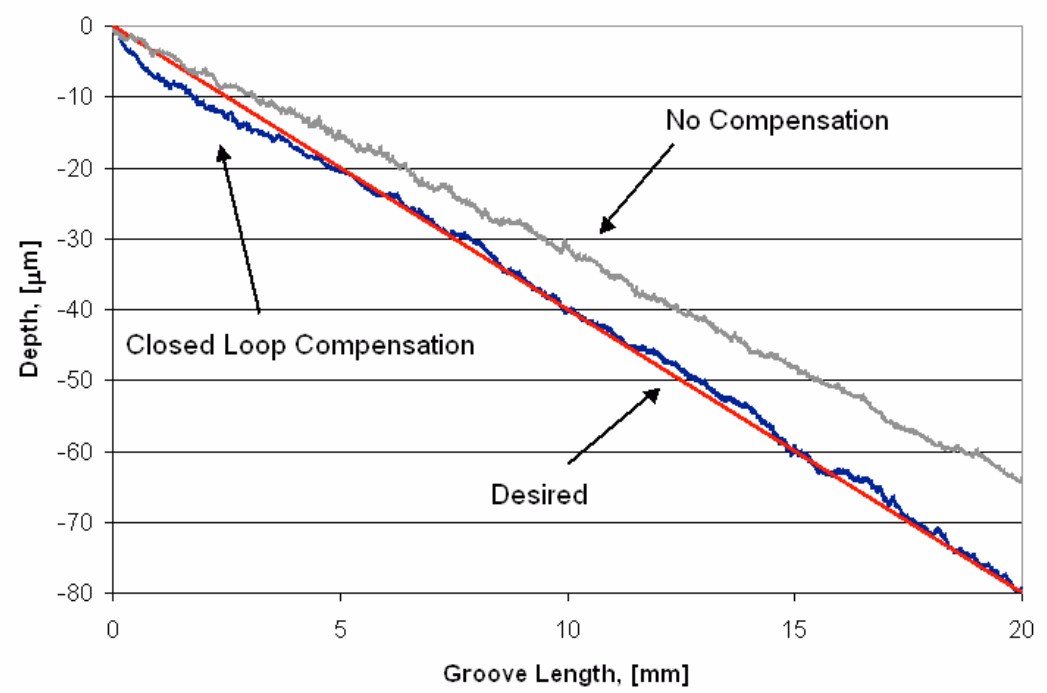

Figure 9. Desired, Spindle Feedback and No Compensation Profiles, Tilt = 30º, Depth = 0-80 mm, Upfeed = 10 mm/rev, Spindle Speed = 10,000 rpm, 4 mm long tool shank

7.4 CONCLUSIONS

Force feedback using either the workpiece or the spindle mounted force gage improved the fidelity of the grooves machined in S7 steel samples. The error was reduced from 16 μm to less than 2 μm over the 80 μm deep, 20 mm long grooves. The limit of the correction using this technique has not been determined but nonlinear effects between force and deflection will ultimately set the best possible compensation.

BIBLIOGRAPHY

1. Hood, David, “Force Feedback Control of Tool Deflection in Miniature Ball End Milling”, MS Thesis, NC State University, June, 2003.
2. Clayton, Stuart, “Force Modeling and Deflection Compensation of Miniature Ball End Mills”, MS Thesis, NC State University, July, 2003.

8 FORCE FEEDBACK DEFLECTION COMPENSATION OF MINIATURE BALL END MILLS

Karl Freitag
Graduate Student
Ryan Huth
Undergraduate Student
Thomas Dow
Professor, Mechanical and Aerospace Engineering

8.1 INTRODUCTION

The primary objective of this research is to improve dimensional tolerances and reduce cycle time of precision milling operations through the development of force-feedback machining. Force-feedback machining uses real-time force measurement to provide active error compensation of tool deflection. Present research focuses on force-feedback machining using miniature (< 1 mm diameter) ball end mills because of the significant tool deflection for radial cutting loads. When this force-feedback loop is operational, the tool deflection will be compensated by increased depth of cut and the result will be improved form error of the machined part.

8.2 PZT ACTUATED SPINDLE

A piezoelectrically actuated spindle was designed and built by Stuart Clayton for active error compensation of tool deflection. Forces, which were initially taken from a load cell mounted under the workpiece, could now be measured at the spindle and corrected using the actuator. In this design, the spindle is supported at two points, a pair of actuators at the front and a single 3-axis load cell at the back as shown in Figure 1. The actuator also has a capacitance gage for displacement feedback to correct for hysteresis in the piezoelectric material. Based on calibration and the mechanical advantage due to the distance between actuator and tool tip, the measured forces are turned into commands to extend the actuator and correct for the tool deflection.

There were several problems that became apparent while using this device. The preload plate at the front of the spindle was intended to apply a compressive load on the actuator to avoid damage for high frequency commands. Unfortunately, it also placed a moment on the structure and influenced the load measured on the load cell. Another problem was the stiffness of the actuator mounting created an upward force on the load cell when the actuator was extended. To compensate for this force, cap gage position was used to measure the piezo extension and an

actuator force was calculated and subtract from the total reading. However, these calculated forces contained errors due to piezoelectric hysteresis and the non-linear relationship between cap gage position and actuator force. In addition to the actuator influence, vibration on the spindle contributed to additional signal noise that also had to be considered. While all these problems were satisfactorily addressed (See Section 7 by S. Clayton), a new design was developed.

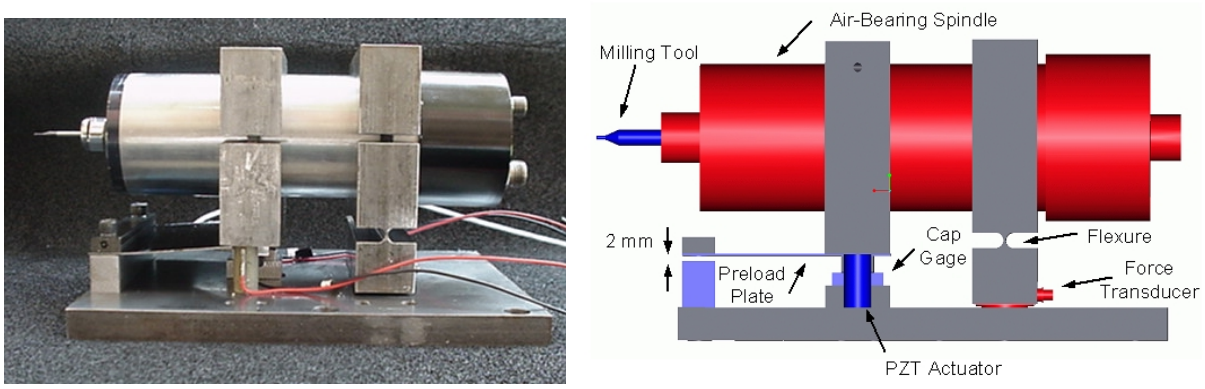

Figure 1. PZT Actuated Spindle

8.2.1 DUAL LOAD CELL SPINDLE

To remove the influence of the actuator on the machining force measurements, a dual load cell spindle was designed and constructed. The goal of this new design (shown in Figure 2) was to separate the force measurement from the actuation process. The spindle was supported using a pair of 3-axis loadcells spaced evenly about the center of gravity of the spindle and mount. Two load cells were used for several reasons. With a loadcell at only one support, only a fraction of the total load was measured because the actuator supported part of the load. This measurement was then multiplied by a scaling factor to obtain the cutting force. In the spindle design of Figure 1, less than 20% of the total load was supported at the loadcell, decreasing the sensitivity of the measured force. When the load cell reading was scaled to determine the input force, signal noise (spindle vibration, actuator influence, electrical noise) were amplified as well. Another advantage to the two load cell design was that vibration of the spindle could be measured and removed from the force measurements. With two load cells evenly supporting the load, common motion of the spindle created by rotational effects could be eliminated by comparing the readings.

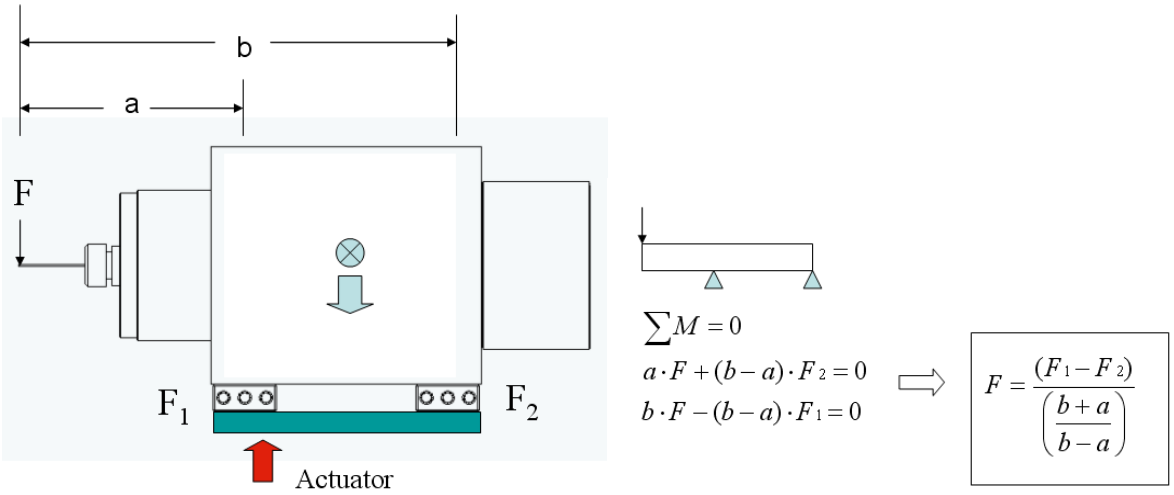

Figure 2. Dual Load Cell spindle and Static Equations

8.2.2 DUAL LOAD CELL STATIC CALIBRATION

To calibrate the dual load cell, the spindle was incrementally loaded in each of the X,Y and Z directions with the load located at the tool tip. The corresponding load cell readings were recorded and slopes calculated for the responses in each direction of loading. Based on the slopes calculated for each direction, three simultaneous equations were solved to calculate the input force from the resulting X, Y, and Z load cell readings.

$$A = \begin{bmatrix} a & b & c \\ d & e & f \\ g & h & i \end{bmatrix} = \begin{bmatrix} 0.8874 & 0 & 0 \\ 0 & 2.9904 & 0 \\ 1.3603 & 0.1625 & 3.2699 \end{bmatrix}$$

$$\begin{bmatrix} L_x \\ L_y \\ L_z \end{bmatrix} = \begin{bmatrix} a \cdot F_x & b \cdot F_y & c \cdot F_z \\ d \cdot F_x & e \cdot F_y & f \cdot F_z \\ g \cdot F_x & h \cdot F_y & i \cdot F_z \end{bmatrix} \qquad F = \begin{bmatrix} F_x \\ F_y \\ F_z \end{bmatrix} \qquad B = \begin{bmatrix} L_{x1} + L_{x2} \\ L_{y1} - L_{y2} \\ L_{z1} - L_{z2} \end{bmatrix}$$

$$AF = B$$

$$F = A^{-1}B$$

$$\begin{bmatrix} F_x \\ F_y \\ F_z \end{bmatrix} = \begin{bmatrix} 1.127 & 0 & 0 \\ 0 & -.3344 & 0 \\ -.4688 & -.0166 & .3058 \end{bmatrix} \begin{bmatrix} (Lx_1 + Lx_2) \\ (Ly_1 - Ly_2) \\ (Lz_1 - Lz_2) \end{bmatrix}$$

First three equations were written for each of the load cell directions. These equations expressed the load measured in each direction X, Y, Z as a function of three input forces Fx, Fy, and Fz.

The linear factors a, b, c, … i were obtained by loading the spindle in one direction at a time where the other two input forces are zero. In these equations the Lx represents the load cell readings and the Fx represents the input forces on the tool.

Solving these three equations simultaneously, results in an expression for the input forces Fx, Fy and Fz as a function of the load cell readings. The resulting equations were then verified by loading the spindle at various angles. The system was able to determine both the input force and the direction of the load placed at any angle.

8.2.3 DYNAMIC RESPONSE OF SPINDLE

When the static equations described above are applied to cutting forces measured during a machining experiment, the resulting calculated forces Fx, Fy, and Fz are larger than the forces measured using a load cell behind the workpiece. These forces are amplified due to the dynamic response of the spindle as it is subjected to a forced vibration at the cutting frequency. Figure 3 is a graph of the resulting ratio between the workpiece measured cutting forces and the spindle load cell measured forces in the same direction by spindle speed.

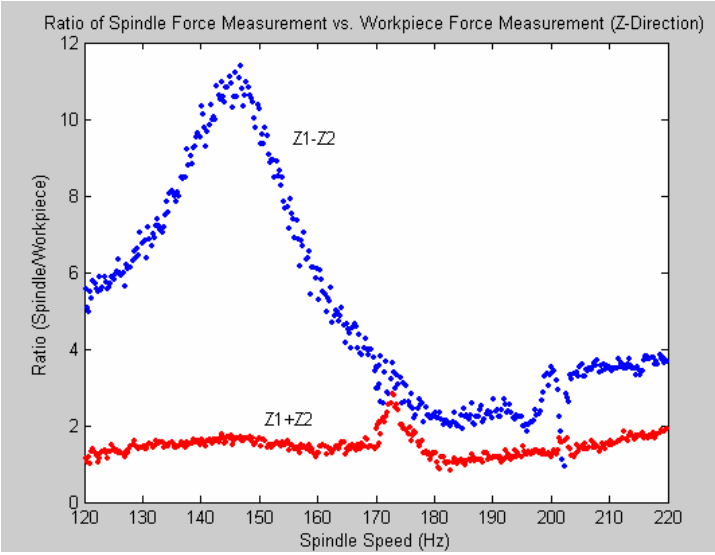

Figure 3. Ratio of spindle measured Force to workpiece Force

To accurately use the spindle load cell measurements, the correct dynamic magnification factor must be used based on the spindle speed. It can also be seen that the ratio is more consistent when looking at the sum of the two loadcell readings rather than the difference because the spindle is being forced in a “rocking” mode during the cutting process.

8.3 CONCLUSIONS

Separation of the actuator from load cell measurement is essential for obtaining accurate cutting force measurements on the spindle. Using two load cell supports insures that all forces are captured and no assumptions or estimations of force need to be made. Proper interpretation of the spindle load cell readings must be made based on spindle speed to obtain accurate force measurements.

Future work includes determination of the dynamic magnification factors for all three directions X,Y,Z on the spindle. Using the appropriate factors and using the workpiece loadcell the measured forces can be compared. This comparison will serve for verification that the cutting forces are being accurately measured on the spindle. Upon achieving accurate cutting force measurements on the spindle will be the addition of a 1-D actuator, and finally the addition of the 2-D actuator.

BIBLIOGRAPHY

1. Clayton, S., "Force Modeling and Deflection Compensation of Miniature Ball End Mills" MS Thesis, North Carolina State University, 2003.

2. Dow, T., Miller E., Garrard K., Sohn A., Wright, T. "Compensation of Tool Force in Small Diameter End Mills," ASPE Proceedings, Vol. 20, pp. 546-550 and to be published in Precision Engineering in 2003

3. Miller, E., "Deflection Prediction and Error Correction of High Speed Miniature Milling Tools," MS Thesis, North Carolina State University, 2000.

4. Arcona, C., "Tool Force, Chip Formation and Surface Finish in Diamond Turning," Ph.D. Dissertation, North Carolina State University, 1996.

9 SURFACE DECONVOLUTION FOR DIAMOND TURNING

Witoon Panusittikorn
Graduate Student
Kenneth Garrard
Precision Engineering Center Staff
Thomas A. Dow
Professor, Department of Mechanical and Aerospace Engineering

9.1 INTRODUCTION

The dynamics of an electro-mechanical system will create a difference between the input waveform and the output motion. If the system is a Fast Tool Servo (FTS), this difference will produce a form error on the machined surface. An open-loop control approach using an inverse dynamics algorithm, known as deconvolution, for a desired motion path can reverse the effects of attenuation and phase yielding a significant reduction in steady-state form errors as described in the 2002 Annual report [1].

Figure 1 shows the comparison between the output errors of the Variform fast tool servo when the desired output is used as the input (Unmodified) and when the deconvolution algorithm is used to account for the the Variform dynamics. The output motion follows the desired path with less than 10 µm error after a startup interval lasting approximately 4 ms. The system works well at low amplitudes (70 µm) and high frequencies (300Hz) but at both high amplitude (400 µm) and frequency, the Variform cannot accelerate to the desired velocity resulting in errors with respect to the desired excursions.

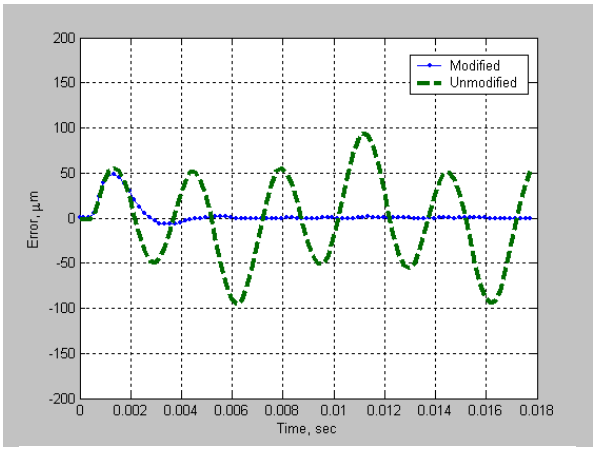

Figure 1. Position errors associated with modified and unmodified inputs

9.2 VELOCITY SATURATION OF THE VARIFORM FTS

Limitations of the deconvolution technique appear when the desired shape has a combination of high frequencies and large amplitudes. Actuator motion is constrained by the maximum velocity of the electro-mechanical system. Figure 2 shows that the Variform with the modified input cannot follow the desired excursion where the velocity exceeds 140 mm/sec. The velocity

saturation reshapes the response associated with a sinusoidal input into a triangle-like signal (top of Figure 3) with the maximum velocity as shown at the bottom of Figure 3. The effects of the distortion on the measured impulse response employed in the deconvolution technique to the operating range of the Variform is explained in the next section.

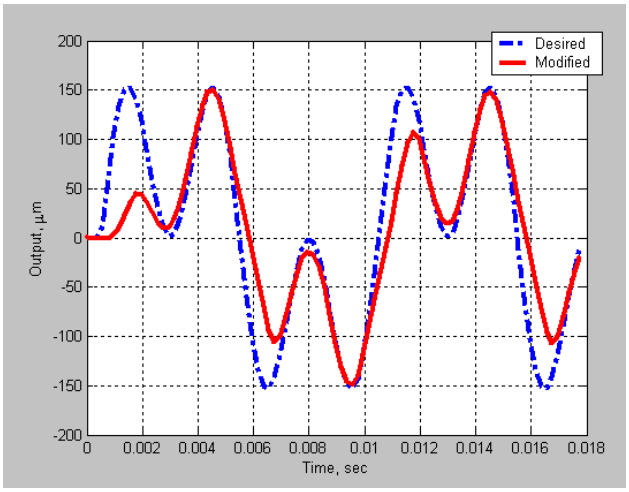

Figure 2. FTS response with respect to high frequencies and large amplitudes input signal.

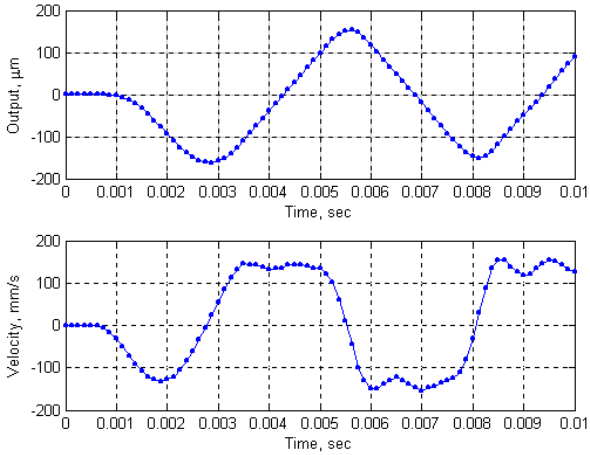

Figure 3. FTS response associated with 200 Hz, 300 µm P-P input signal and its velocity.

9.2.1 OPERATING RANGE

In Figure 4(a), the shape of the FTS output is compared with the shape of the desired excursion and explains the transformation to the more triangular shape. The lower figure illustrates the frequency spectrum of the output profile and that includes the frequency component of the desired tool path (200 Hz) as well as the 3rd and the 5th harmonics, 600 and 1000 Hz respectively. Figure 4(b) shows all of the frequency components of the Variform response and how they combine to create the output motion. The 3rd harmonic is out-of-phase with the base frequency adding to the peak and subtracting in the wings to transform the output to a triangle-like profile. Note that the amplitude of this base frequency is smaller than the amplitude of the distorted output excursion. The difference is **Δ**.

The amplitude difference (**Δ**) has a direct effect on the accuracy of the impulse response measurement that is used to determine the dynamic response of the actuator. The spectrum analyzer (Stanford SR780) generates a varying frequency input with fixed amplitude to the FTS, and analyzes the attenuation and phase of the tool motion captured by an LVDT internal to the FTS at each input frequency. If the output signal is velocity-saturated, its frequency component associated with the input frequency appears as smaller than the actual output signal. As a result, the frequency response of the Variform shows more attenuation than really occurs. Figure 5 depicts the attenuation of the Variform as a function of frequencies and input amplitudes.

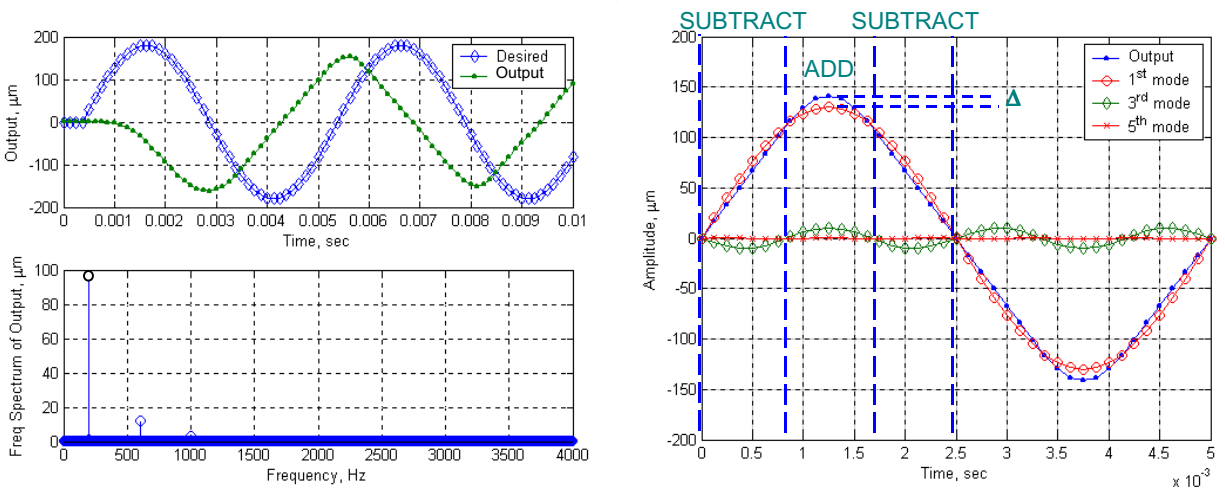

a) b)

Figure 4. a) Time response and frequency spectrum, b) Assembly of the frequency components with respect to the FTS output

The frequency response shows significant attenuation where the input signal contains large amplitudes with high frequencies. This implies that the operating range of the FTS is limited to a velocity below 140 mm/sec as depicted in Figure 6.

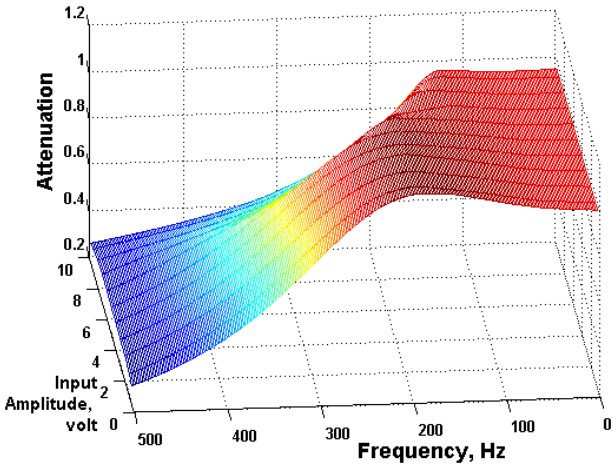

Figure 5. Variform 3D frequency response.

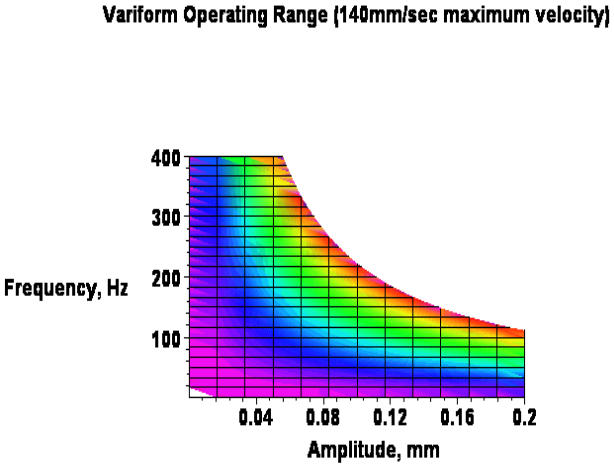

Figure 6. Operating range of the Variform.

9.2.2 DECONVOLUTION IN REAL-TIME

Since an open-loop control approach using an inverse dynamics algorithm, or deconvolution can be performed once for a given set of machining parameters (e.g., spindle speed, cross-feed), the command signal needed to machine a surface can be generated off-line. The deconvolution of the entire tool excursion requires a feedback controller to deal with parameter variations during machining. In practice, a Diamond Turning Machine (DTM) maintains spindle speed using an internal PID controller. Nevertheless, the initial machining parameters can be unintentionally altered while continuously machining surfaces for long period of time. Robustness to the

parameter variations is not guaranteed, as the entire command signal is deconvolved using a fixed set of parameters.

One solution to this problem is to run the deconvolution in *real time*; that is to continuously update machining parameters in the deconvolution calculation. The desired path of the FTS can be defined as a function of the spindle encoder of the DTM. As the spindle speed changes, the time period of the desired path is also altered. This *real time* technique allows the machining parameters to be continuously tuned for an optimal system response. For instance, the spindle speed and cross-feed can be adjusted to maximize the utilization of a FTS within its operating range resulting in a faster production and less form error.

In *real time*, a long tool path must be divided into short pieces that are individually modified using the deconvolution technique. While the Variform follows the current input command, the next piece (or window) of the desired path will be modified using the most recent parameters. This *real time* deconvolution can be achieved by using a window function[1] applied to a long path signal. In general, the window is short in length for sensitivity to high frequency signals. Figure 7 demonstrates how the window function operates using a rectangular window and triangular window to draw a short piece out of a long sinusoidal signal. Those short pieces are transformed to the frequency domain [2] to calculate the inverse dynamics. The transform using window functions is called Short-Time Fourier Transform (STFT) [3-4]. The reverse process, an overlap-add method is used to reconnect those short pieces after deconvolution. Figure 8 shows a schematic of connecting windows as each piece of the next modified tool path overlaps with the present. The short signals combine with the overlaps of the adjacent pieces resulting in a magnified input profile as shown in Figure 9. Note that the reconstructed signal is distorted at both ends as a result of window shapes and the overlap-add method.

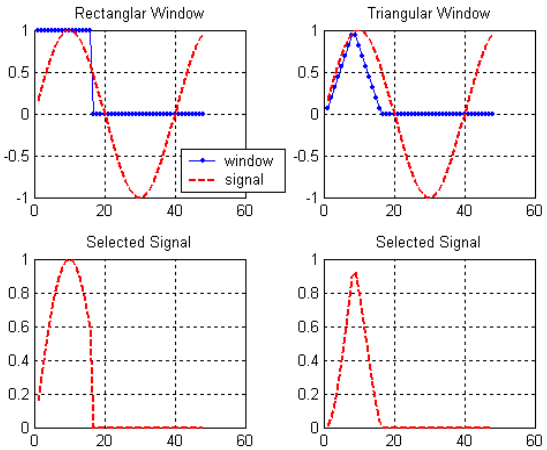

Figure 7. A window (rectangle and triangle) draws out a short piece of the long signal.

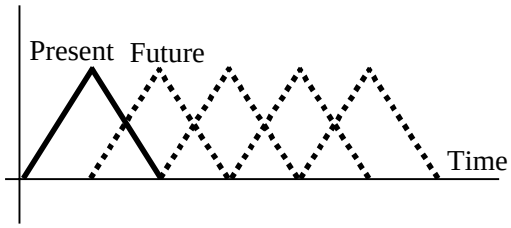

Figure 8. Schematic of connecting windows.

[1] A window function is a set of weight coefficients, which are zero everywhere but in a certain length.

Figure 10 shows the resynthesis process of a sinusoid. In Figure 10(a), a series of windowed signals (lines with dots) are trimed off the left end (lines with circles) to seamlessly connect to the preceding pieces. The entire reconstructed signal is illustrated in Figure 11(b).

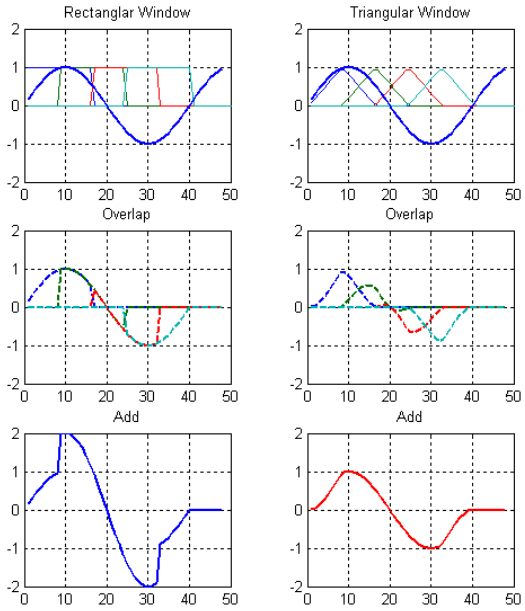

Figure 9. Overlap-add method reconstructs the original signal from small pieces.

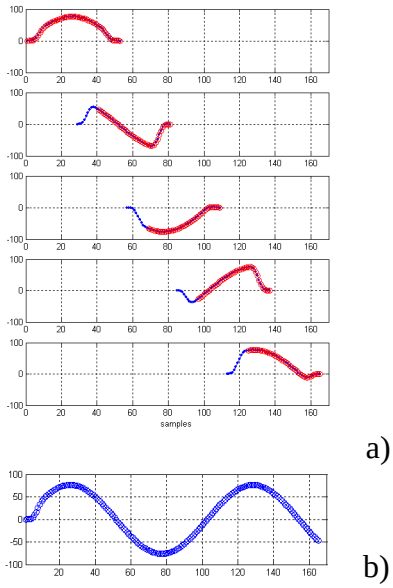

Figure 10. a) Series of synthesized signals associated with windows, b) Entire resynthesized signal.

9.2.3 RESULTS

Experiments were implemented on MATLAB/Simulink with Real-Time Workshop toolbox and a dSPACE (RS1104) data acquisition board. The desired path and machining parameters were uploaded to a Simulink model, which performs the *real time* deconvolution. The tool excursion is windowed, transformed to the frequency domain, modified by the inverse dynamics algorithm, resynthesized, and conveyed to the FTS as a modified input command.

The theoretical response of the Variform associated with the altered amplitude and phase of the modified input is compared to the desired tool path in the form of an error plot in Figure 11(a). The desired motion involves two frequencies (90 and 270 Hz) each with amplitude of 90 μm PP. The error associated with the modified signal experiences short distortion at the initial state due to the weight coefficients of the window function and evolves to a steady state error less than 2 μm in less than 0.025 sec. The experimental measurement of this same desired output is shown in Figure 11(b). The output excursion is essentially in-phase with the desired tool path; however, the amplitude is slightly mismatched and the error is slightly larger than the theoretical predictions.

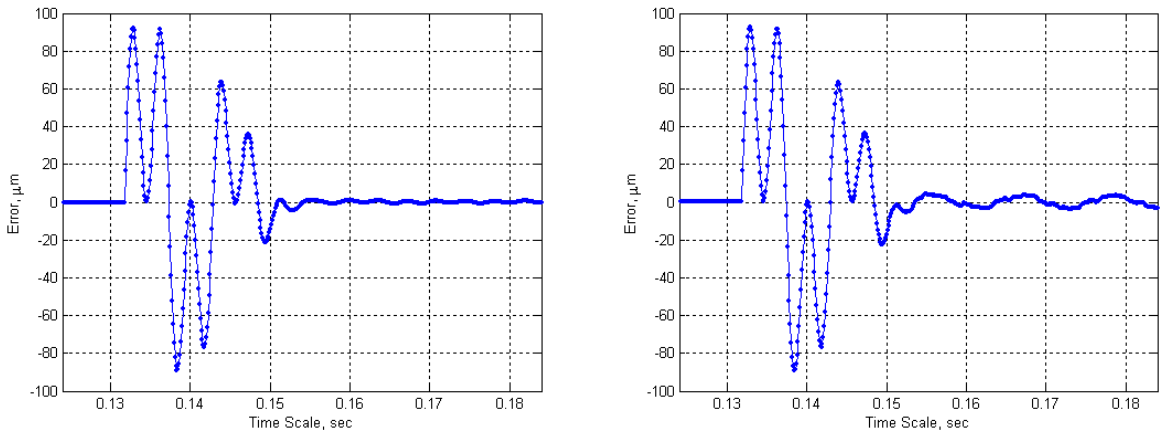

a) b)

Figure 11. a) Desired tool path of 180 µm P-P, 90 and 270 Hz and the Variform response, b) Path difference with respect to the desired excursion

9.3 CONCLUSIONS

An inverse dynamics scheme has been incorporated into a *real time* MATLAB application to correct attenuation and phase using varying machining parameters. The technique "levels up" the machining process by allowing the parameters to be modified to optimize machining conditions resulting in faster production with less form error. The optimal machining conditions assure that the Variform Fast Tool Servo functions within its operating range at a velocity that must be less than 140 mm/sec.

Fundamental concepts of the Fourier Transform in cooperation with window functions (Short-Time Fourier Transform) were introduced to formulate the *real time* corrective algorithm. The open-loop control scheme was implemented in a Simulink environment. Steady-state form errors associated with a modified input signal are significantly reduced after a startup interval approximately 0.025 second. Experiments show similar results to the simulation. The Variform phase delay is essentially reduced to zero after the start up interval.

REFERENCES

1. Panusittikorn, W., and K. Garrard, *Surface Decompositon for Diamond Turning.* Precision Engineering Center Annual Report, 20, pp 117, (2002).
2. Oppenheim, A.V., and R.W. Schafer, *Discrete-Time Signal Processing.* Prentice Hall, pp 541, (1998).
3. Lim, J.S., and A.V. Oppenheim, *Advanced Topics in Signal Processing.* Prentice Hall, pp 289, (1987).
4. Quatieri, T.F., *Discrete-Time Speech Signal Processing.* Prentice Hall, pp 309, (2001).

10 ELLIPTICAL VIBRATION ASSISTED DIAMOND TURNING

Nobuhiko Negishi
Graduate Student
Thomas A. Dow
Professor, Mechanical and Aerospace Engineering

10.1 INTRODUCTION

Fabrication of optical quality surfaces on non-ferrous materials can be produced with single crystal diamond tools and precision turning machines. To add ferrous and brittle materials to the list of diamond turnable materials, a process know as Elliptical Vibration Assisted Machining (EVAM) is being developed. The PEC has built an EVAM system known as the UltraMill [1] that combines a small elliptical tool path (40 µm horizontal by 6 µm vertical at 600 v excitiation) to the linear motion of standard orthogonal cutting. EVAM reduces cutting forces and tool wear by reducing chip thickness and keeping the tool tip out of contact with the workpiece for 75% of the time. These characteristics increase tool life and expand work piece material compatibility with single crystal diamond tools.

10.2 SURFACE ROUGHNESS MEASUREMENTS

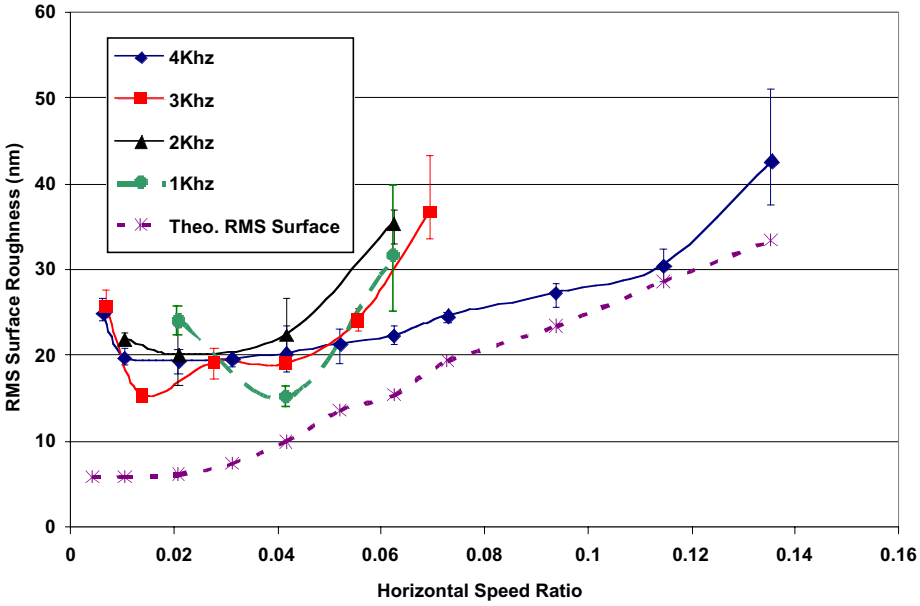

Figure 1. Surface Roughness as a Function of HSR on PMMA
(100 rpm Spindle Speed, 1.25 mm/min Cross Feed, 12.5 µm/rev)

The surface roughness of the EVAM machining experiments was compared to a theoretical prediction for grinding surface finish developed at the PEC by Storz [2]. This comparison is illustrated in Figure 1. Here the areal RMS roughness as measured on a Zygo New View is plotted as a function of the Horizontal Speed Ratio (HSR) for different EVAM frequencies. The HSR is the ratio of the maximum speed of the elliptical motion to the surface speed of the part and is proportional to the distance that the part moves for each elliptical cycle of the tool. The model tracks the experiments well above 7% HSR but below that value the experiments seem to reach a plateau of 20 nm while the predicted value drops to 5 nm. The speed of the EVAM motion (1-4 KHz) does not seem to affect the minimum roughness.

The 20 nm limit was the result of 60 Hz asynchronous surface features produced on the part. Since the **x** and **y** carriages of the Diamond Turning Machine (DTM) have a natural frequency of 60 Hz and 90 Hz respectively, these features were originally thought to be caused by machine vibration introduced by the inertial forces of the UltraMill or by ancillary components such as the cooling system pump. Following a series of experiments designed to isolate the source of this vibration, the Kinetic Ceramics amplifiers were found to be defective; introducing noise spikes of 25 nm magnitude at a period of 16 msec (60 Hz) into the drive signal. Trek P1019 (PZD500) dual channel piezo drivers were loaned by Precitech for further experiments. These amplifiers were capable of producing a clean drive signal of 600 volts peak-to-peak but were limited to 1 KHz. The measured RMS surface roughness for an EVAM turned part is plotted in Figure 2 as a function of HSR.

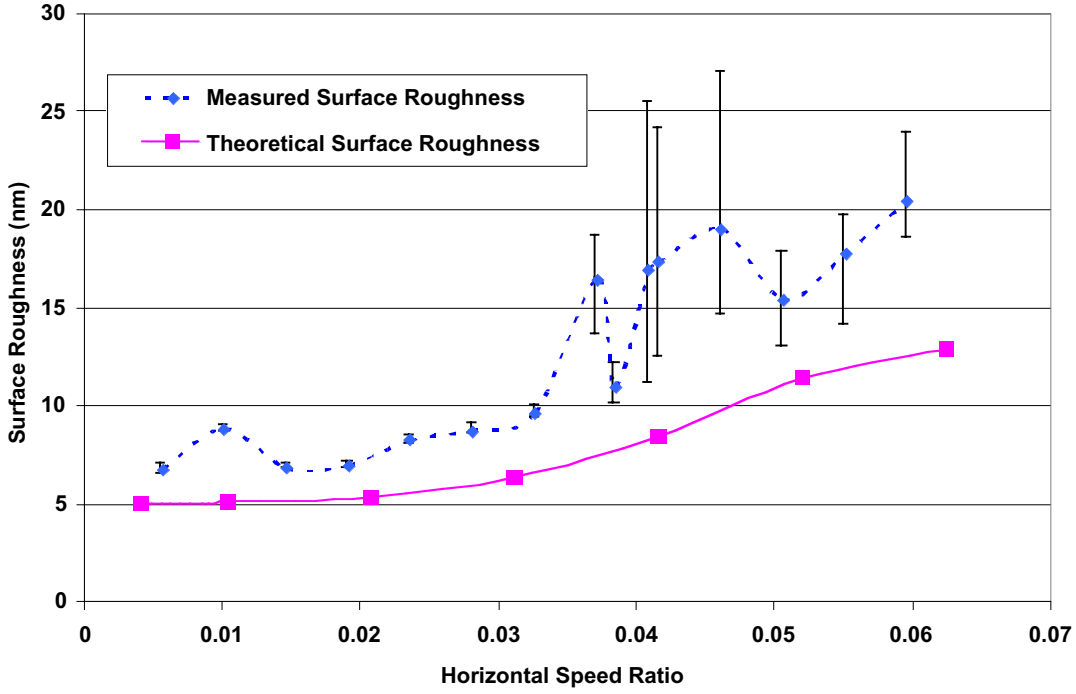

Figure 2. Measured and Theoretical Surface Roughness on PMMA
(1 Khz, 21.4 rpm, 0.25 mm/min, 12 µm/rev)

The minimum theoretical surface roughness values were calculated using the Storz's method [2] and the theoretical values are the smallest possible from the model. The general trend of the measured roughness curve follows the theoretical behavior. The 20 nm limit is no longer observed in these results where the minimum measured surface roughness is 6.5 nm RMS. The surface finish experiments showed that EVAM features could be predicted from the elliptical tool path and tangential workpiece velocity.

10.3 SIC MACHINING EXPERIMENT

The groove cutting experiment described in the 2002 Annual Report proved that the EVAM process could be used to machine SiC; however, creating an optical surface is a more challenging problem. To demonstrate the possibilities, the UltraMill was used to machine a surface with a 1 mm outer radius and a 0.5 mm inner radius. The fracture data from the groove cut experiment showed that damage free surfaces could be machined if the chip thickness is less than 20 nm. This value was used to determine the cutting conditions at the outer radius of the machined surface where the upfeed – and therefore the chip thickness – is the largest. The UltraMill was operated at 1 KHz and 600 volts peak-to-peak using the Trek amplifiers to create the 40 x 6 μm ellipse. The tool was fed across the part at 12 μm per revolution. The part rotated at 1 RPM and the maximum HSR, occurring at a radius of 1 mm, was 0.08%.

10.3.1 APPARATUS

The SiC specimen was vacuum mounted to the DTM spindle using a custom, diamond turned fixture. The workpiece velocity required for the desired maximum chip thickness at a 1 mm radius was determined to be 0.1 mm/s, or approximately 1 RPM. The motor for the DTM cannot operate at such a slow speed so the spindle was driven by a stepper motor through a flexible rubber belt. The SiC specimen was 25.4 mm square by 0.8 mm thick with a polished surface of less than 0.5 nm RMS over an area of 0.0156 mm^2. The surface of the unmounted specimen had a spherical shape with a P-V of 10 μm. Once supported on the vacuum chuck, the surface flatness was less than 600 nm over the area to be machined. Based on this runout, the desired nominal depth of cut was set at 600 nm.

10.3.2 MACHINING PROCEDURE

The UltraMill was operated at 1 Khz for 40 minutes to allow the temperature to equilibrate. After the equilibration period, the tool was brought into contact with the rotating specimen at a radius of 0.4 mm. The tool tip was positioned to within several micrometers of the surface as observed with a telescope and moved in 100 nm increments until a chip was created. The oil jet was activated and the part program was run. The machining process required 44 minutes, during which the temperature of the UltraMill piezo stacks dropped by 0.4˚C. The goal for the touch off

technique was to avoid depths of cut greater than 1.2 µm. The measured depth of cut for the surface ranged from 30 nm to 418 nm with an average depth of 300 nm.

10.3.3 SURFACE MEASUREMENTS

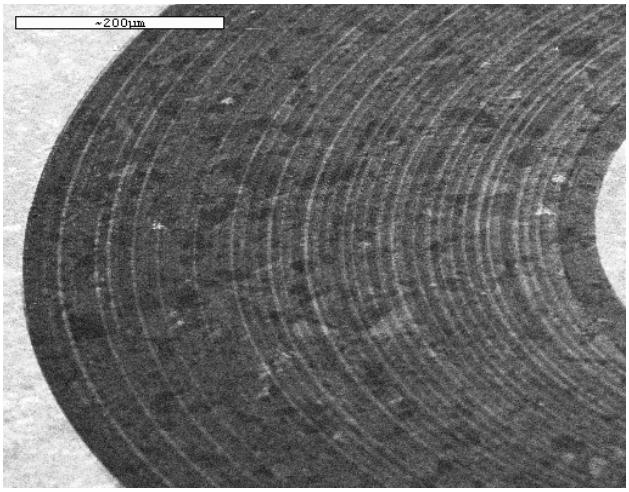

Figure 3. SEM Micrograph of SiC Surface

Figure 3 is an SEM micrograph of the machined surface of the SiC. The nominal cutting distance was 196.25 mm and the volume removed was $7x10^{-4}$ mm^3 with a removal rate of 15,900 μm^3/min. The average of the tangential and radial profiles and surface measurements are plotted as a function of radial position in Figure 4. The machined SiC surface has an average roughness of approximately 8 nm RMS. The theoretical RMS roughness of the machined surface is dominated by the cross feed and has a value of 5.5 nm. The theoretical roughness along the groove bottom is 1 angstrom. This value is much less than the spindle error motion and therefore is not visible. The value shown in Figure 4 is equal to the average spindle error.

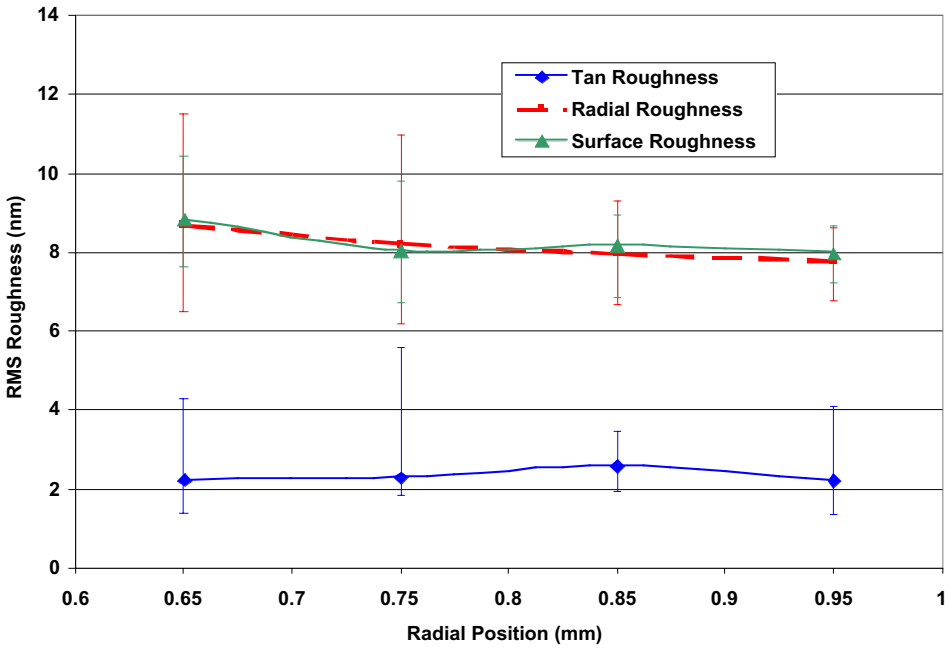

Figure 4. Surface Measurements of Machined SiC CVD
(1 rpm spindle speed, cross feed = 12 µm, upfeed = 40 nm, frequency = 1 Khz)

Figure 5 is a Zygo contour image of the machined surface at a radius of 0.85 mm. The cross feed marks can be clearly seen at 12 µm spacing. Normally these would be connected by vertical

lines due to the upfeed motion created by the elliptical motion of the tool. However, for this experiment, the upfeed rate of 40 nm/cycle is beyond the resolution of the instrument. What are visible are lower frequency vibrations attributed to spindle and DTM slide motion. A trace along one of the grooves has amplitude of 2.5-5 nm at a frequency of 25 Hz. Surface roughness along the machined groove is 1.9 nm RMS. Some surface damage was noted and can be seen along the bottom of one of the up feed grooves.

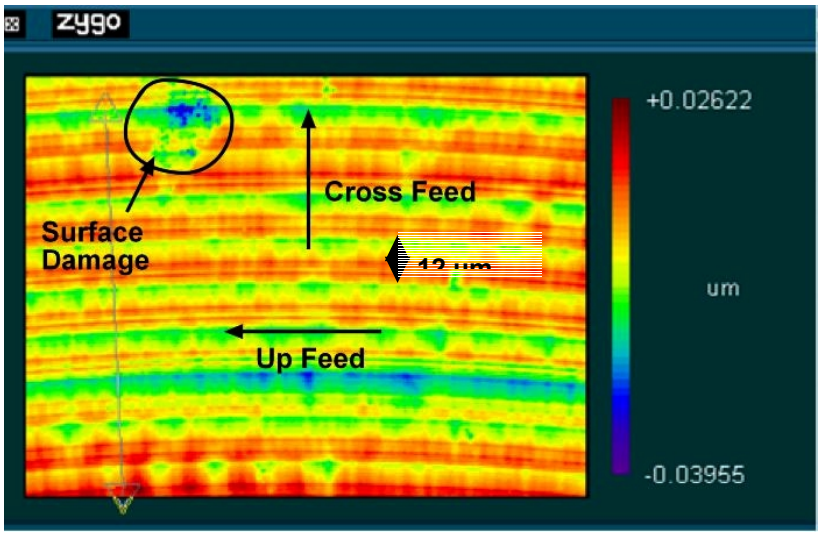

Figure 5. Contour Plot of EVAM Surface in SiC (HSR=0.08%)

A profile trace in the cross feed direction (Figure 6) provides another view of the surface. This scan reveals a cross feed period of approximately 11.9 µm and a local feature height of 16 µm. These values are similar to the theoretical 12 µm cross feed and 18 µm peak-to-valley feature height. The cross feed features have distinct, repeated characteristics which are believed to be the result of features on the tool edge being imprinted on the SiC surface during machining. These features appear to be small fractures or damage sites, less than 5 nm deep.

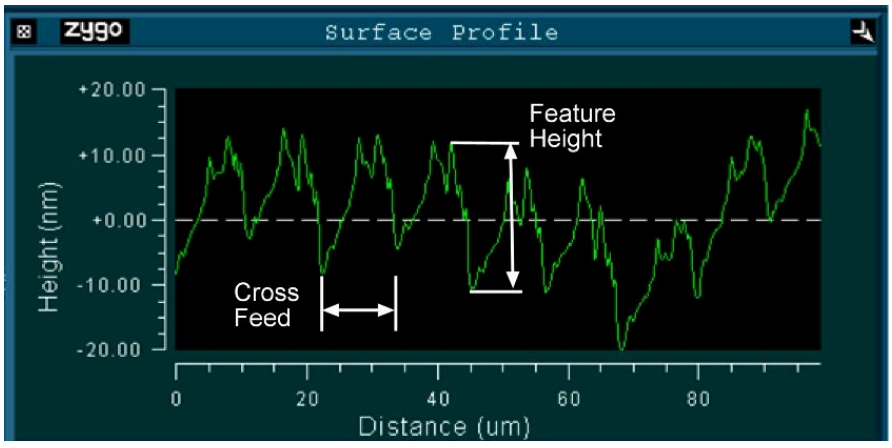

Figure 6. Radial Profile of SiC Surface (Cross Feed = 12 µm/ rev)

10.4 TOOL WEAR

SEM micrographs of the tool tip before and after the machining process reveal visible wear. The cutting edge was imaged with the SEM before machining the SiC and is shown on the left side of Figure 7. There appears to be no visible damage to the edge. After machining the SiC, the tool edge was again inspected with the SEM. No indication of tool wear could be found on the rake face; however, the flank face revealed features shown at the right of Figure 7. The width of the worn area is the same as the theoretical contact length of 25 µm for a 1 mm radius tool at a depth of 300 nm. This correlation suggests that this wear area was created during the machining process.

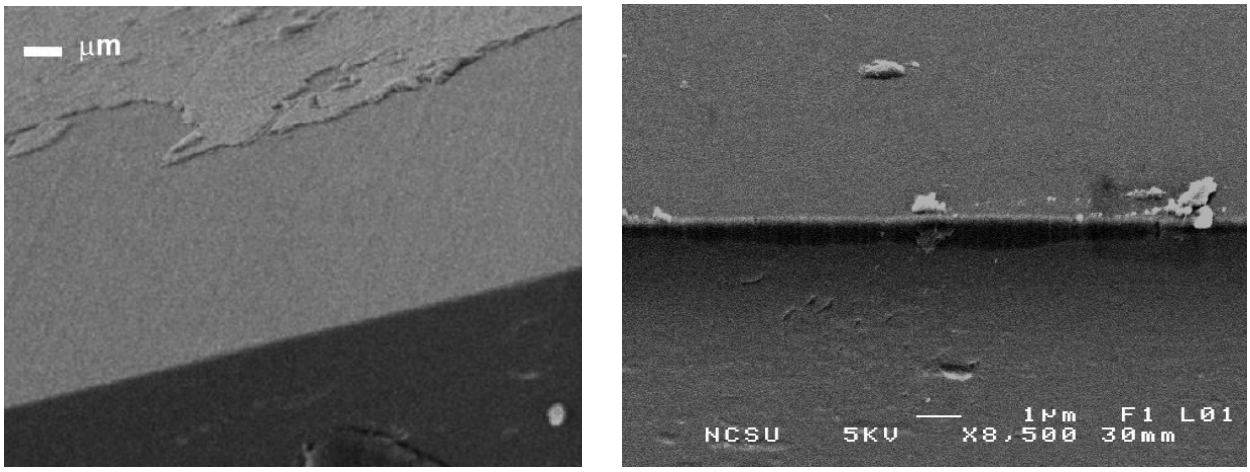

Figure 7. Worn and Unworn Tool Edge

A close up view of the flank wear region in Figure 8 shows wear patterns and striations in the upfeed direction as expected. The length of the wear land is approximately 400 nm. Given this wear land and a clearance angle of 10.4˚, a rake face recession of 74 nm is estimated. This calculation assumes a flat wear land which may not be the case for the EVAM process.

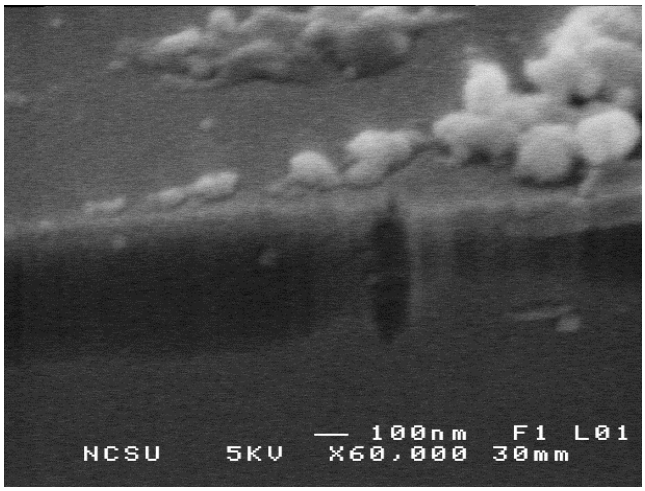

Figure 8. Worn Edge on Diamond Tool

The radial and surface measurements are similar in magnitude, 8 nm RMS, suggesting that the overall surface roughness is mostly a result of cross feed features. This was expected based on the selected machining conditions.

10.5 CONCLUSIONS

The UltraMill is a rugged, reliable design for creating surfaces using elliptical vibration assisted machining. It has two major advantages over previous designs; first, the elliptical motion has a significant vertical component that can be used to control the thickness of the chip; and second, motion of the tool is below the first natural frequency so the speed is easily adjustable from 1-5 KHz. This device has been used to machine a variety of materials, from aluminum to plastics to SiC. It can produce optical quality surfaces and the accompanying tool wear for difficult to machine materials – steel and ceramics – is less than conventional diamond turning.

REFERENCES

1. Negishi, N., "Elliptical Vibration Assisted Machining with Single Point Diamond Tools" MS Thesis, NC State University, 2003.
2. Storz, G. E. II, "Theoretical Modeling of Precision Contour Grinding Operations" MS Thesis, NC State University, 1994.